

FYS4310

Doping Ion Implantation¹²

Fys4310 I², Program

What is I²

How it is done

Characteristics

Ranges

$R=f(?)$, $S_n(E)$, $S_e(E)$ - qualitatively

LSS

Impulse approximation

Examples, measurements

Disorder

Channelling

Annealing of disorder

What is I²

How: See next slide

Characteristics

Energy: 15 keV - 250 keV, (5 keV.. MeV)

Dose: 1e12 - 1e15(1e18) cm⁻²

The benefits of I² technology

Control, reproducibility, uniformity, flexibility

Dose (Q_T) measured accurately by integrating current

High purity obtainable by mass separation

The less ideal things about I² technology

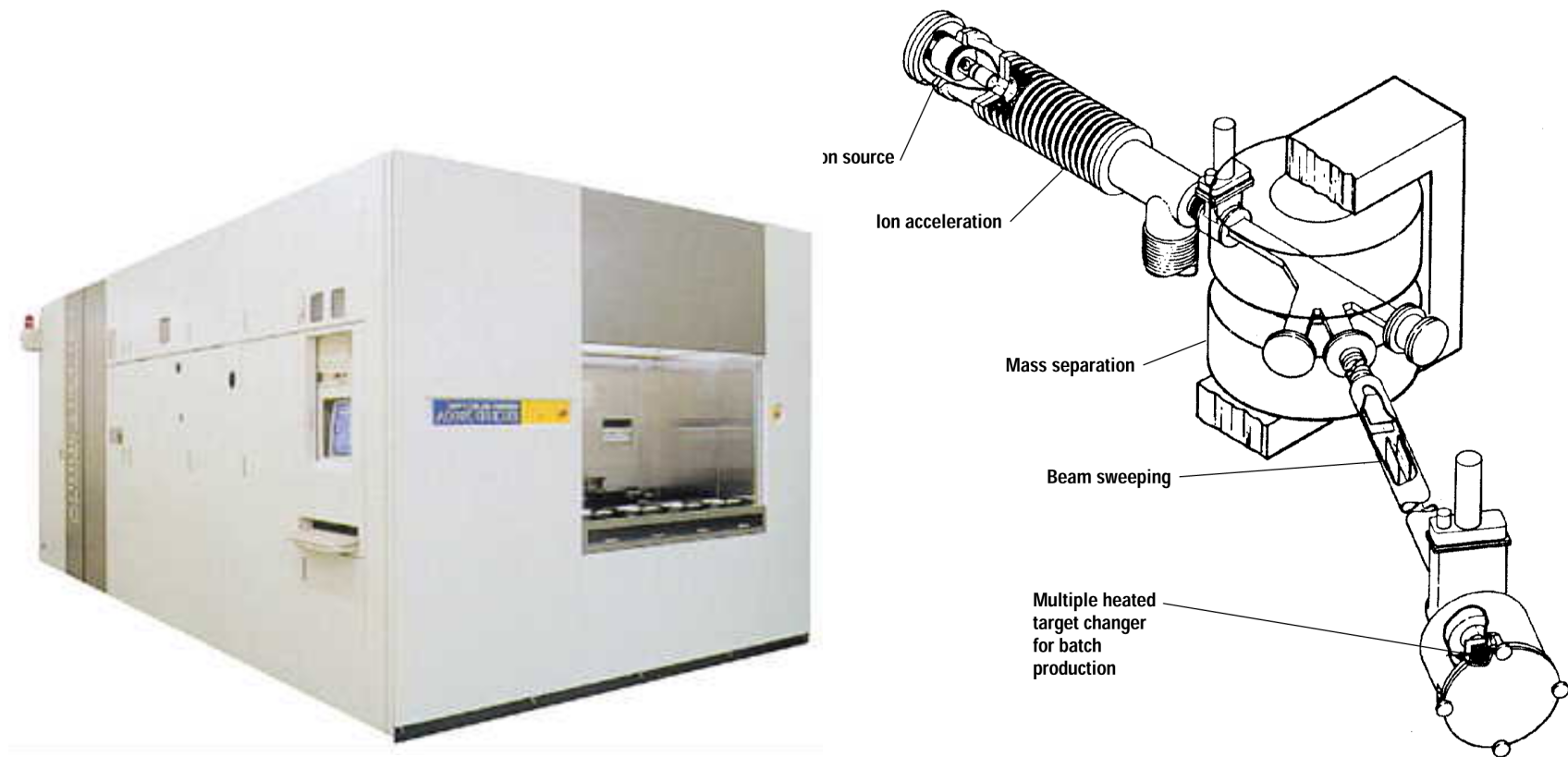
Cost of an ion implanter machine

High throughput; even more expensive

Radiation damage

Impossible to implant delta function/the ultimate shallow profile

The Ion Implanter



Ion implanter in a 'FAB'

Figure 5.1 Schematic of an ion implanter (*after Mayer et al., reprinted by permission, Academic Press*).

Practical equipment related issues

Sector magnet resolving power

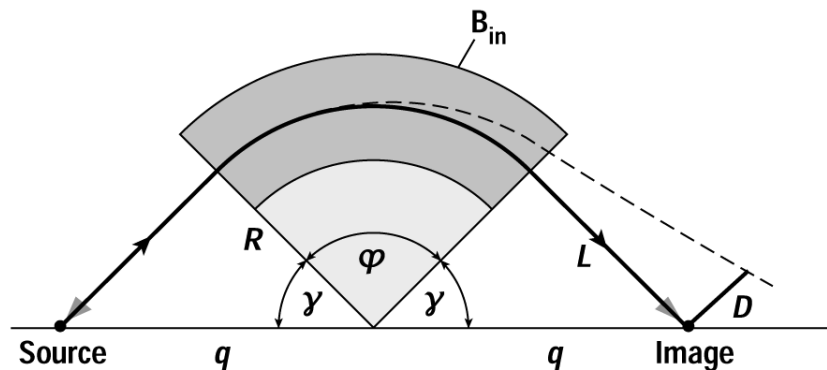


Figure 5.3 Mass separation stage of an ion implanter showing perpendicular magnetic field and ion trajectory. D corresponds to the displacement for an ion of M d. M .

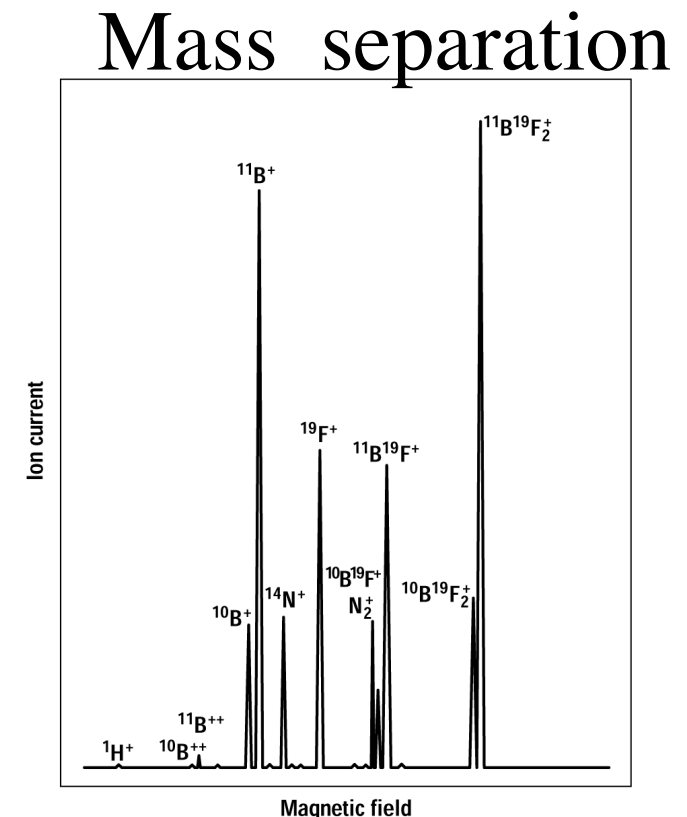


Figure 5.4 Typical mass spectrum for a BF_3 source gas (after Ryssel and Ruge, reprinted by permission, Wiley, see [54]).

Practical equipment related issues. Limitation; implant angle

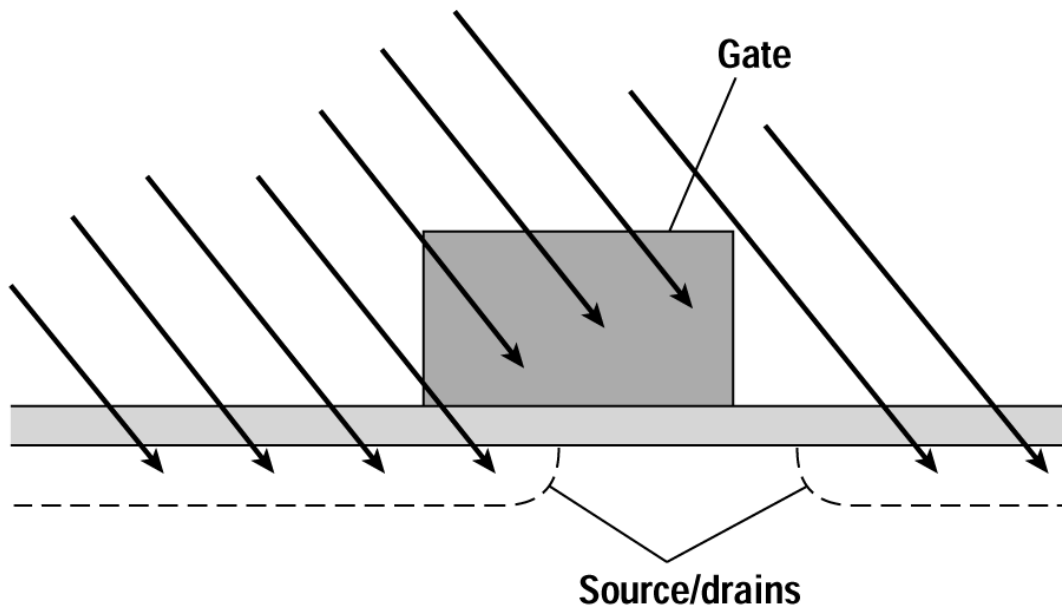


Figure 5.20 Simple shadowing example for deeply scaled MOSFET. As a result of the tilt angle one of the source/drain diffusions does not extend to the channel leading to poor I-V characteristics.

Practical equipment related issues. Limitation, scan angle

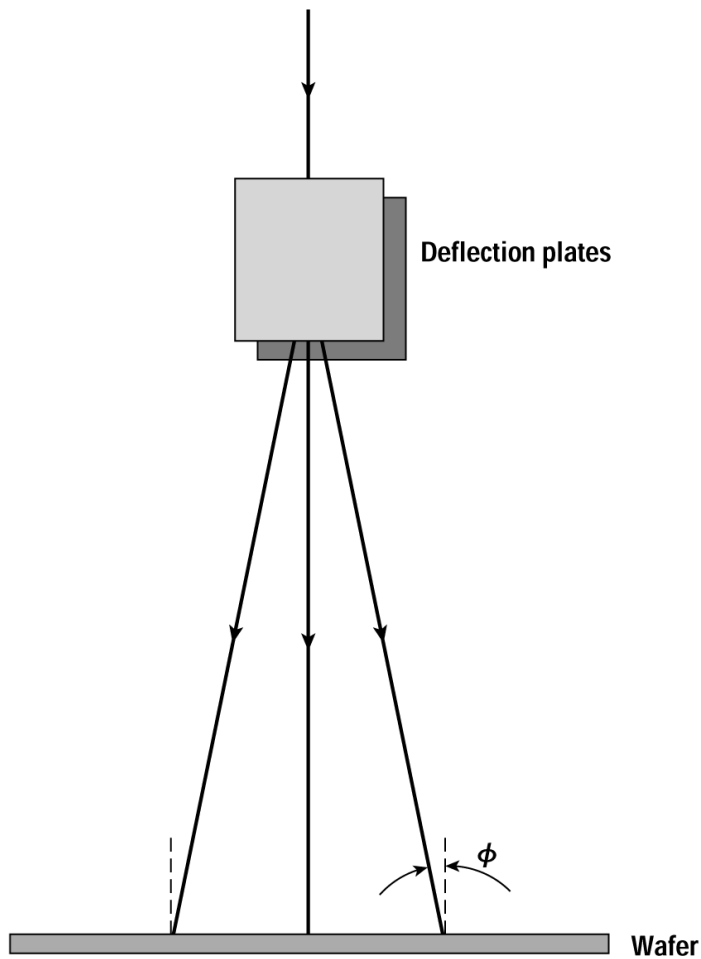


Figure 5.21 Variability of the angle between the incident beam and the surface normal in simple electrostatically scanned systems.

Practical equipment related issues.

Scanneng approaches

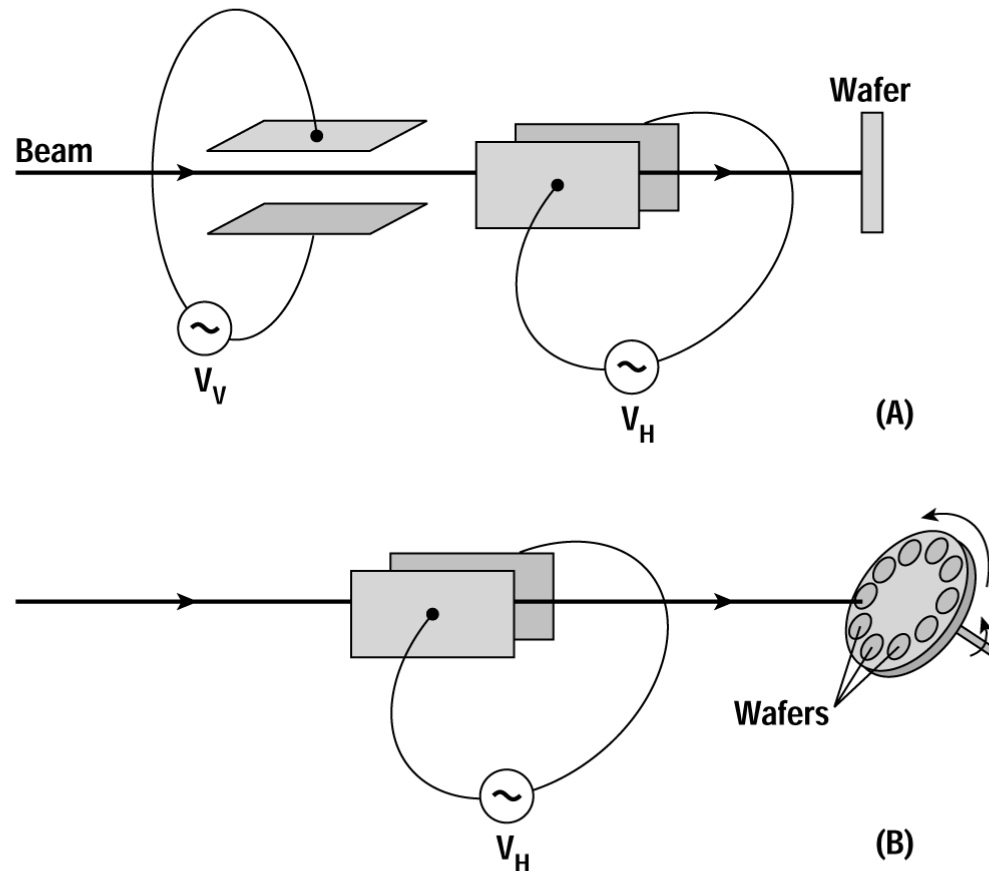


Figure 5.5 Typical scanning systems for ion implanters.
(A) Electrostatic rastering commonly used in medium current machines. (B) Semielectrostatic scanning used on some high current machines.

Ranges, R

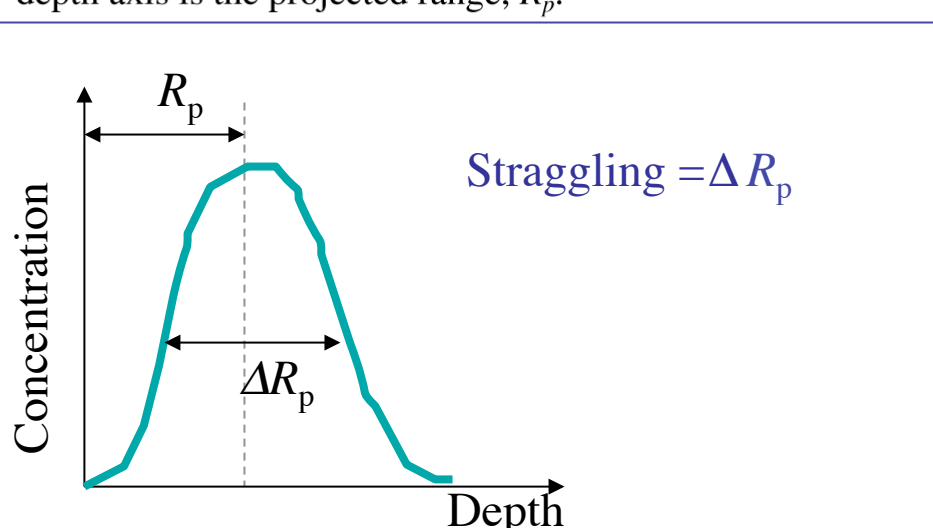
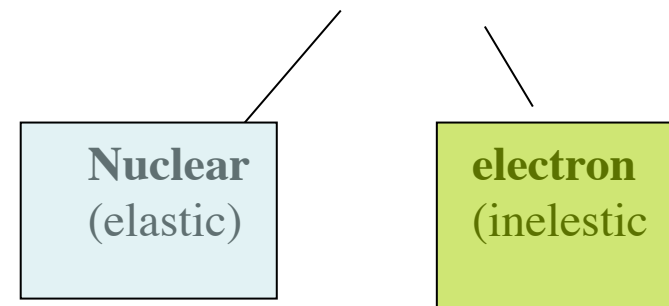
projected range = R_p



Figure 5.7 The total distance that an ion travels in the solid is the range. The projection of this distance along the depth axis is the projected range, R_p .

$$R = \int_E^0 \frac{1}{dE} dE = \int_E^0 \frac{1}{S(E)} dE$$

$$S = S_n + S_e$$



$$S(E), S_n S_e$$

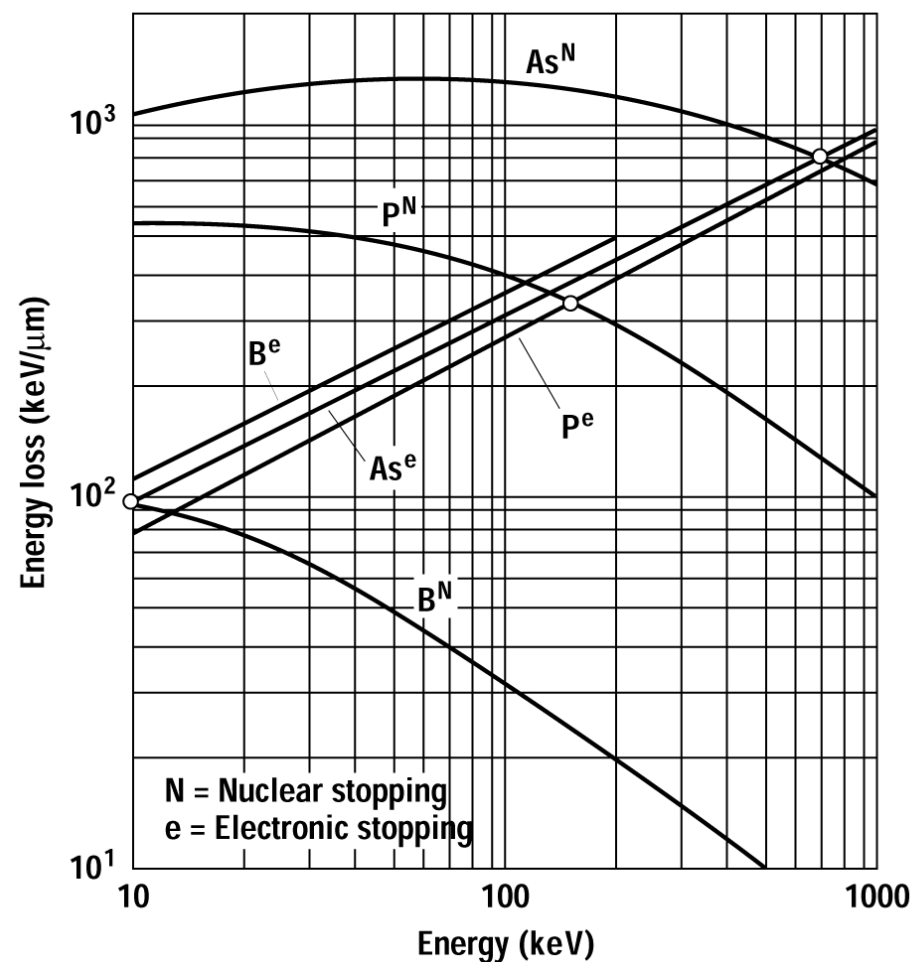
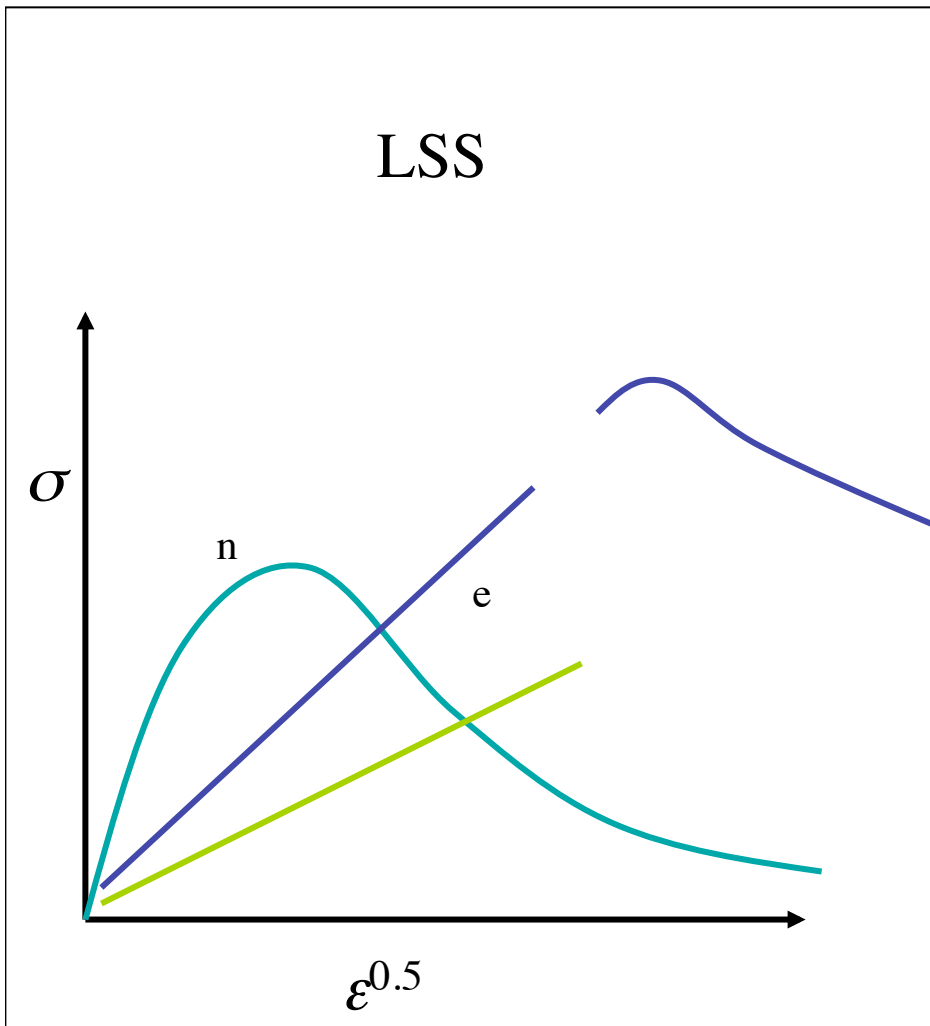


Figure 5.8 Nuclear and electronic components of $S(E)$ for several common silicon dopants as a function of energy (after Smith as redrawn by Seidel, "Ion Implantation," reproduced by permission, McGraw-Hill, 1983).

ion-solid interaction, approximation

Binary collision:

Ok nuclear collisions ,

Not so good at end of the range, E low, then molecular dynamics,
then manybody problem

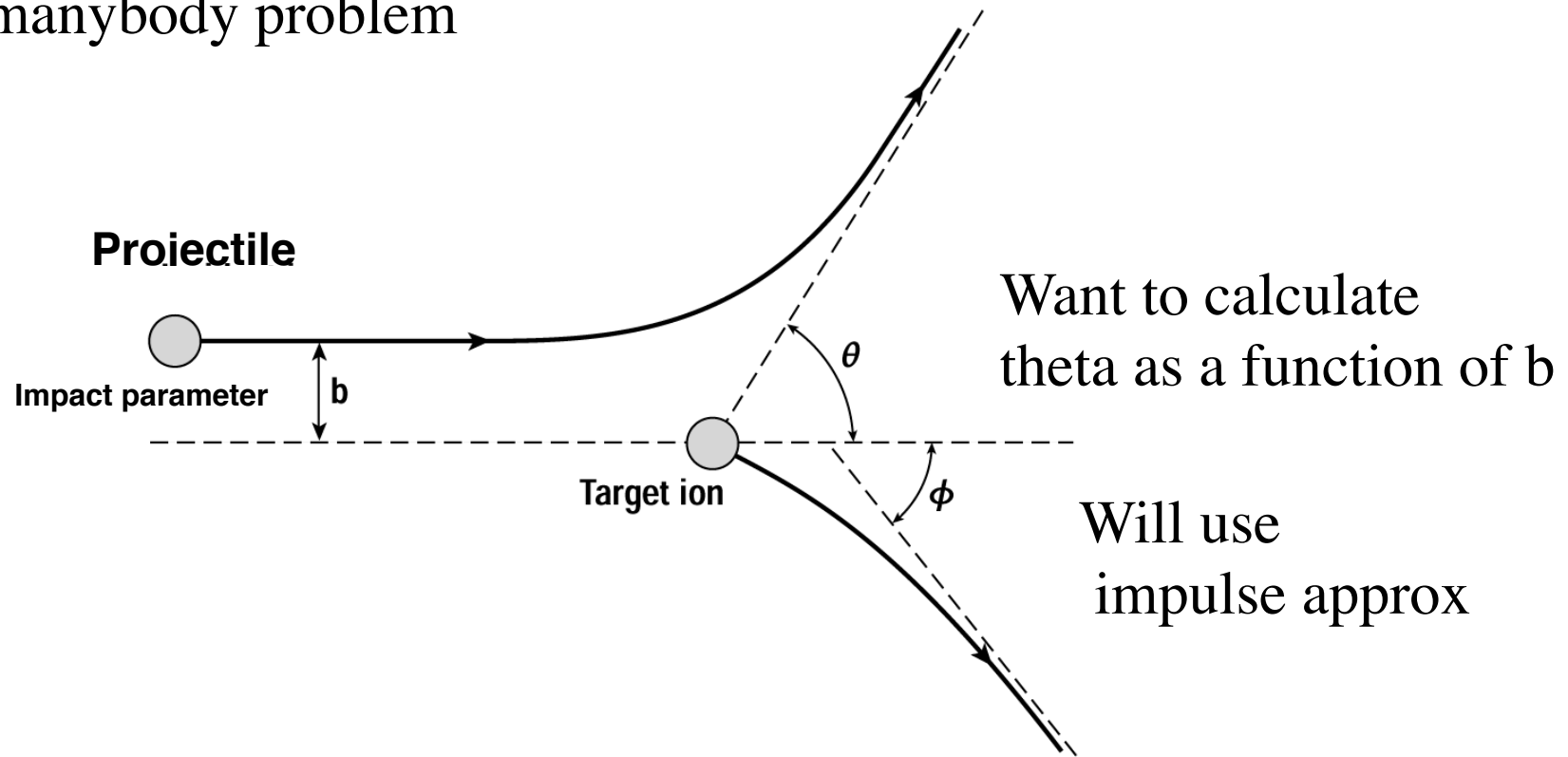
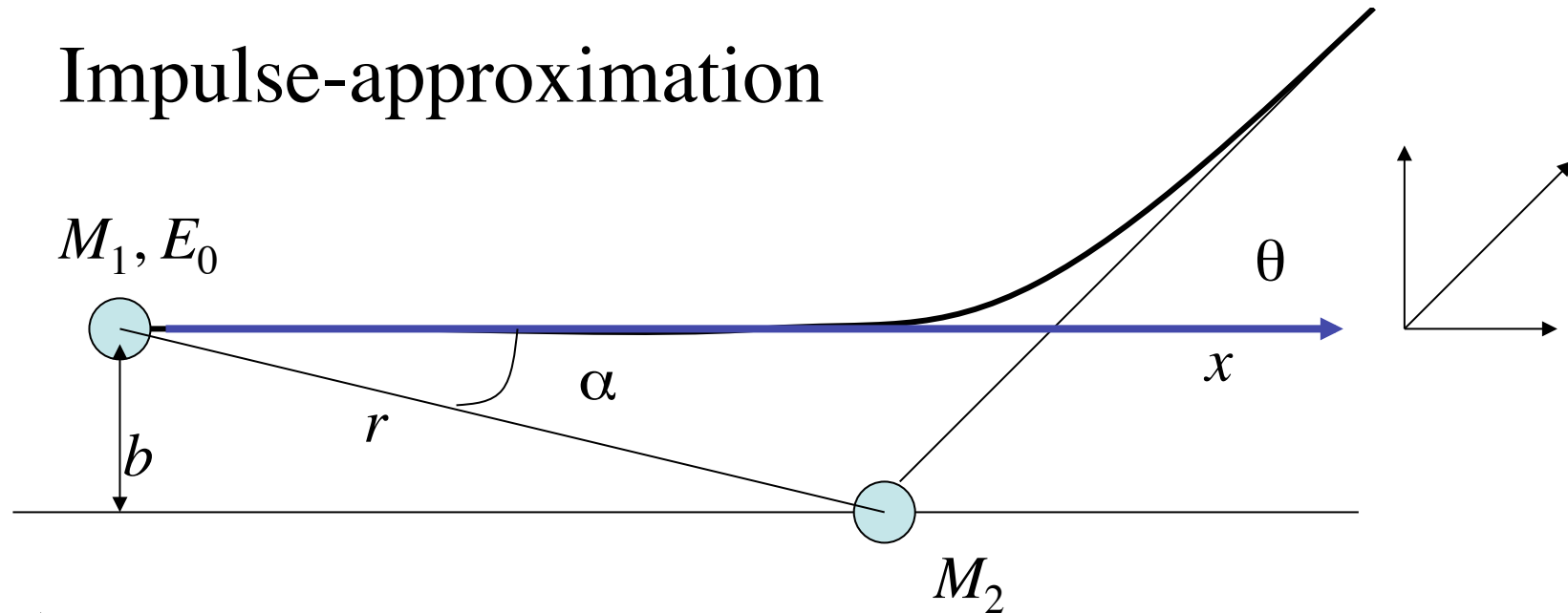


Figure 5.6 Typical scattering problem. Figure inset shows electrostatic potential as a function of distance between the nuclei. The impact parameter is labeled b .

Impulse-approximation



$$\vec{F} = \frac{\partial V}{\partial r} \frac{\vec{r}}{r}$$

The force F acts on the projectile through the traveled distance dx
 The time it takes is $dt = \frac{dx}{v_1}$

$$\vec{F} = \frac{d\vec{p}}{dt} \quad d\vec{p} = \vec{F} dt \quad \text{Integrate } -\infty \dots +\infty. \quad (\text{Momentum change parallel path} = 0)$$

perpendicular:

$$\Delta p = \int dp = \int_{-\infty}^{\infty} -\frac{\partial V}{\partial r} \frac{dx}{v_1} \sin(\alpha) = \left\{ \int F dt \right\} \quad \sin(\alpha) = \frac{b}{r}; dx = r dr (r^2 - b^2)^{-\frac{1}{2}}$$

$$\Delta p = \frac{2}{v_1} \int_b^{\infty} -\frac{\partial V}{\partial r} \frac{b dr}{\sqrt{r^2 - b^2}} \quad \theta \approx \tan(\theta) = \frac{\Delta p}{M_1 v_1}$$

Impulse-approximation, example:Coulomb potential

$$V(r) = \frac{Z_1 Z_2 q^2}{r} \quad 4\pi\epsilon_0 = 1$$

$$\Delta p = \frac{2}{v_1} \int_b^\infty -\frac{\partial V}{\partial r} \frac{b dr}{\sqrt{r^2 - b^2}} \quad \theta = \frac{\Delta p}{M_1 v_1}$$

$$\Delta p = \frac{2 Z_1 Z_2 q^2}{v_1 b}$$

$$\Delta p_{lab} = \Delta p_{CM} \quad v_{1CM} = \frac{M_2}{M_1 + M_2} v_{o,lab}$$

$$\theta_{CM} = \frac{\Delta p_{CM}}{m_1 v_{1CM}} = \frac{2 Z_1 Z_2 q^2}{v_o b (M_1 + M_2) v_o} = \frac{Z_1 Z_2 q^2 (M_1 + M_2)}{E_o b M_2}$$

$$b^2 = \frac{(M_1 + M_2)^2 (Z_1 Z_2 q^2)^2}{E_o^2 \theta^2 M_2^2}$$

Impulse-approximation, example Coulomb potential

Transferred energy T

$$T = T_{\max} \sin^2 \frac{\theta}{2} \approx \frac{4M_1 M_2}{(M_1 + M_2)^2} \frac{\theta^2}{4} E_0$$

→ $\theta^2 = \frac{T}{E_0} \frac{(M_1 + M_2)^2}{M_1 M_2}$ Enter this in expression for b

$$b^2 = \frac{(M_1 + M_2)^2 (Z_1 Z_2 q^2)^2 E_o M_1 M_2}{E_o^2 T (M_1 + M_2)^2 M_2^2} = \frac{(Z_1 Z_2 q^2)^2 M_1}{E_o^2 T M_2}$$

$$\sigma(T) dT = -2\pi b db = -\pi d(b^2) = \frac{\pi (Z_1 Z_2 q^2)^2 M_1}{E_o^2 T^2 M_2} dT \quad S_n = 2\pi \int_0^\infty T(b) b db$$

Impulse approximation gives analytical results for potentials of the type $1/r$, $1/r^2$, $1/r^s$,

LSS

Impulse approx. with Thomas Fermi potential

$$V(r) = \frac{(Z_1 Z_2 q^2)}{r} f\left(\frac{r}{a_{TF}}\right)$$

$$a_{TF} = \frac{0.468 \times 10^{-8} \text{ cm}}{\sqrt{Z_1^{2/3} + Z_2^{2/3}}}$$

Reduced parameters

Path length/areal density

$$\rho = f_R(M)R = 4\pi a_{TF}^2 N \left(M_1 M_2 / (M_1 + M_2)^2 \right)$$

energy

$$\varepsilon = f_E(M, Z)E = E(a_{TF}/q^2) \left(M_2 / Z_1 Z_2 (M_1 + M_2) \right)$$

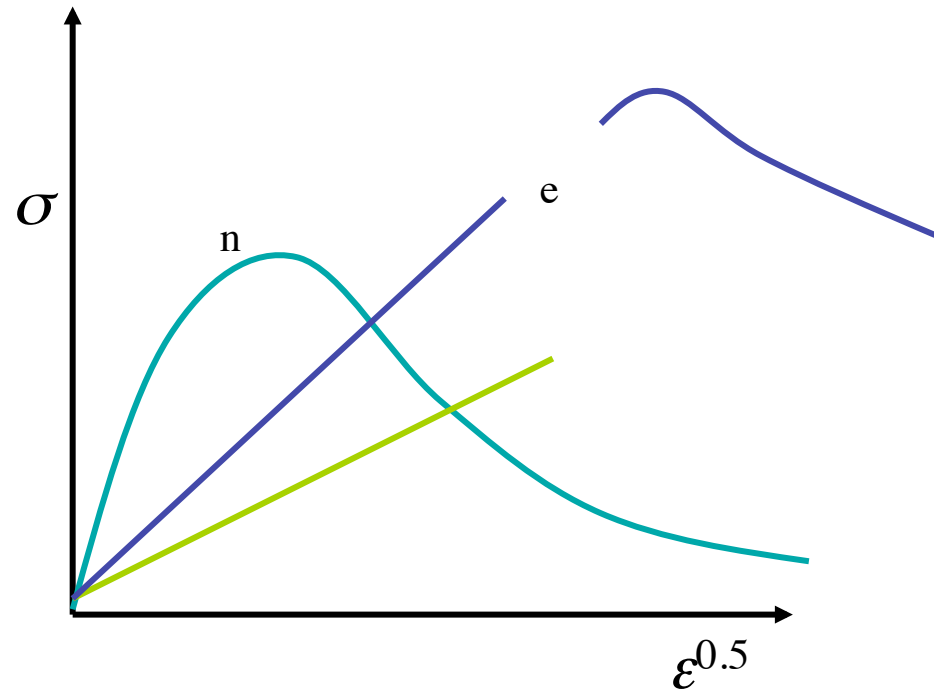
Transferred energy

$$t = f_t(M, Z)T$$

Stopping power

$$\sigma = \frac{\partial \varepsilon}{\partial \rho}$$

Thomas-Fermi screening func.



LSS nuclear and electronic stopping

Stopping Mechanisms

- Electronic collisions dominate at high energies.
- Nuclear collisions dominate at low energies.

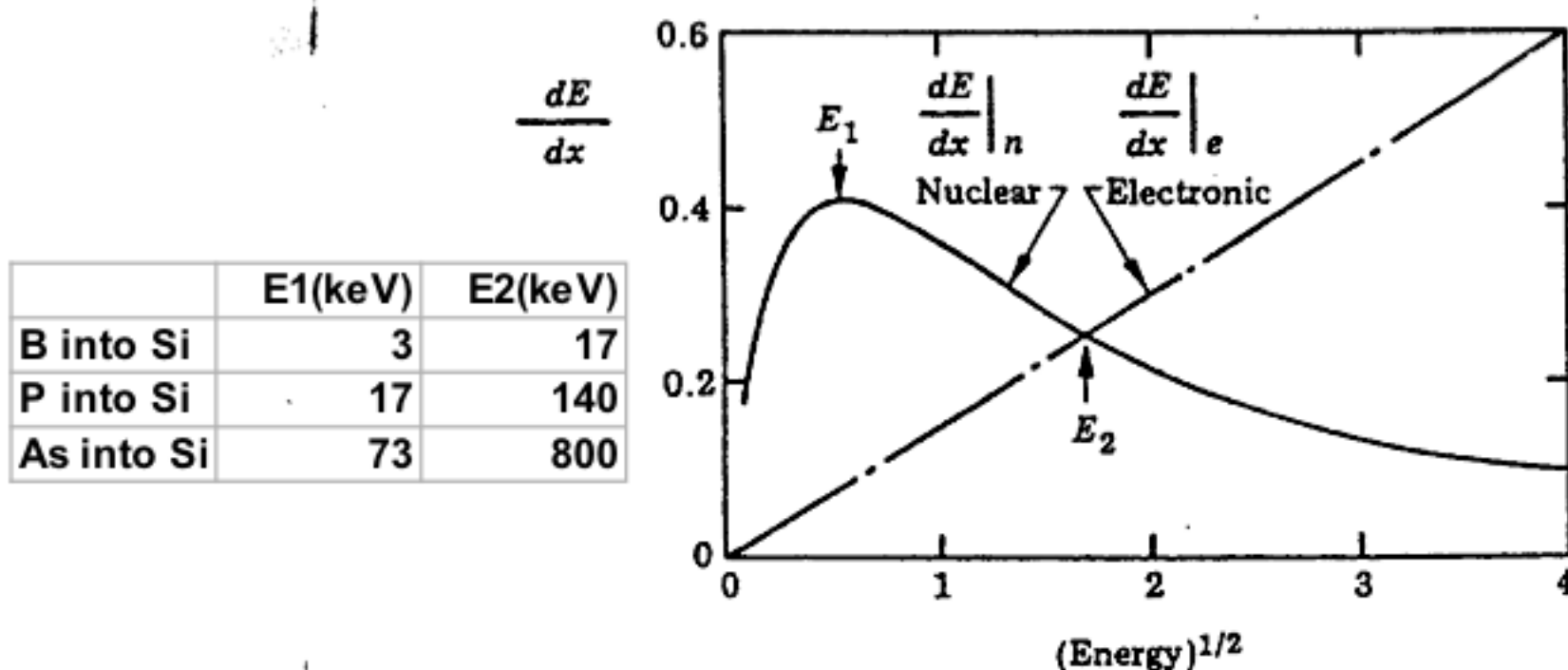


FIGURE 8.12 Rate of energy loss dE/dx versus $(\text{energy})^{1/2}$, showing nuclear and electronic loss contributions.

Implant profiles

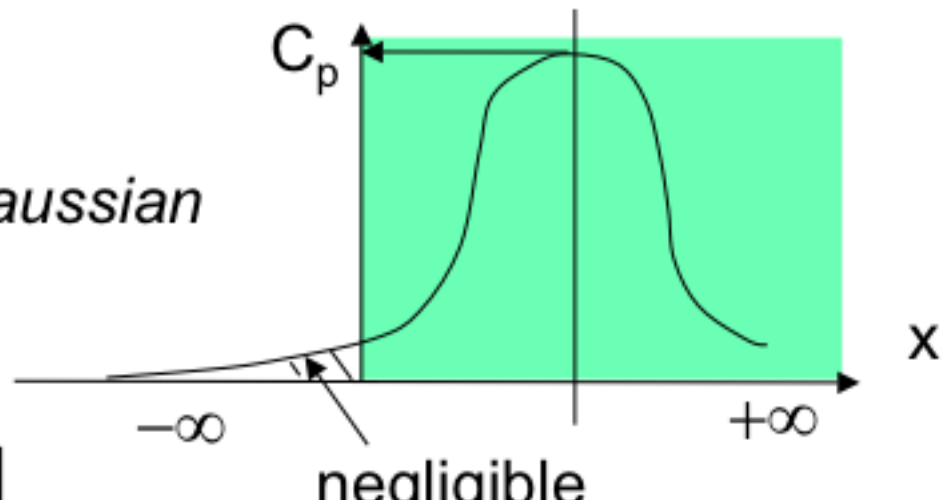
One-Dimensional Implantation Profile Models

(1) Gaussian Distribution

$$\text{Dose} = \phi = \int_0^{\infty} C(x) dx \quad \text{Gaussian}$$

$$\approx \int_{-\infty}^{+\infty} C(x) dx$$

$$= C_p \cdot [\sqrt{2\pi} \cdot \Delta R_p]$$



$$\therefore C_p = \frac{\phi}{\sqrt{2\pi} \Delta R_p} \cong \frac{0.4\phi}{\Delta R_p}$$

Definitions of Profile Parameters

(1) **Dose** $\phi = \int_0^\infty C(x)dx$

(2) **Projected Range:** $R_p \equiv \frac{1}{\phi} \int_0^\infty x \cdot C(x)dx$

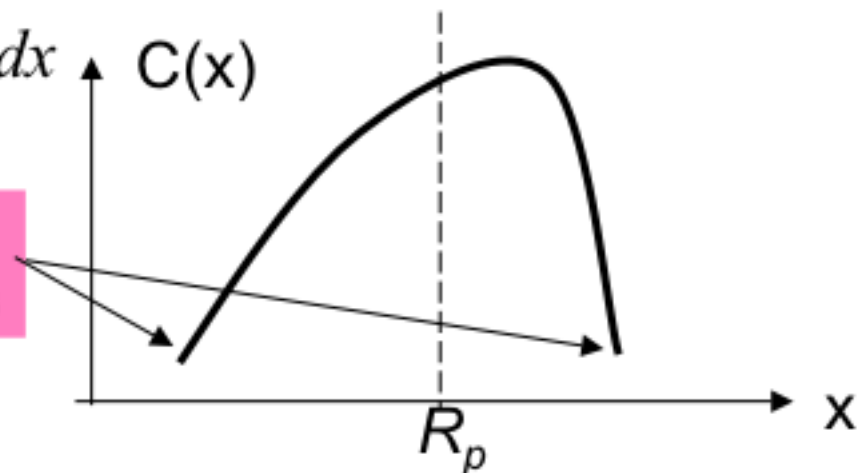
(3) **Longitudinal Straggle:** $(\Delta R_p)^2 \equiv \frac{1}{\phi} \int_0^\infty (x - R_p)^2 \cdot C(x)dx$

(4) **Skewness:** $M_3 \equiv \frac{1}{\phi} \int_0^\infty (x - R_p)^3 C(x)dx \quad M_3 > 0 \text{ or } < 0$

-describes asymmetry between left side and right side

(5) **Kurtosis:** $\propto \int_0^\infty (x - R_p)^4 C(x)dx$

Kurtosis characterizes the contributions of the “tail” regions



Implant profiles

The Pearson Distributions

For reference only

$$\frac{df(s)}{ds} = \frac{(s - a)f(s)}{b_0 + b_1s + b_2s^2} \quad (12)$$

where $s = x - R_p$. The Pearson coefficients can be written in terms of the first four moments of the distribution:

$$a = -\gamma\sigma_p(\beta + 3)/A \quad (13a)$$

$$b_0 = -\sigma_p^2(4\beta - 3\gamma^2)/A \quad (13b)$$

$$b_1 = a \quad (13c)$$

$$b_2 = -(2\beta - 3\gamma^2 - 6)/A \quad (13d)$$

$$A = 10\beta - 12\gamma^2 - 18$$

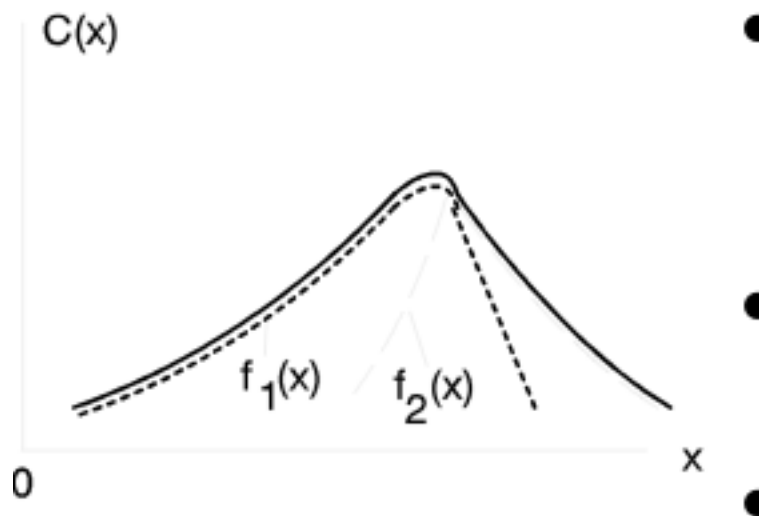
The Pearson-IV Solution (valid if $0 < b_1^2/4b_0b_2 < 1$) Default model for SUPREM

$$\ln\left[\frac{f(s)}{f_0}\right] = \frac{1}{2b_2} \ln(b_0 + b_1s + b_2s^2) - \frac{b_1/b_2 + 2b_1}{\sqrt{4b_0b_2 - b_1^2}} \tan^{-1}\left(\frac{2b_2s + b_1}{\sqrt{4b_0b_2 - b_1^2}}\right)$$

Note: If experimental kurtosis does not satisfy Pearson-IV condition, A **modified** kurtosis $\beta \cong 2.8 + 2.4\gamma^2$ is used to force the fitting.

Implant profiles

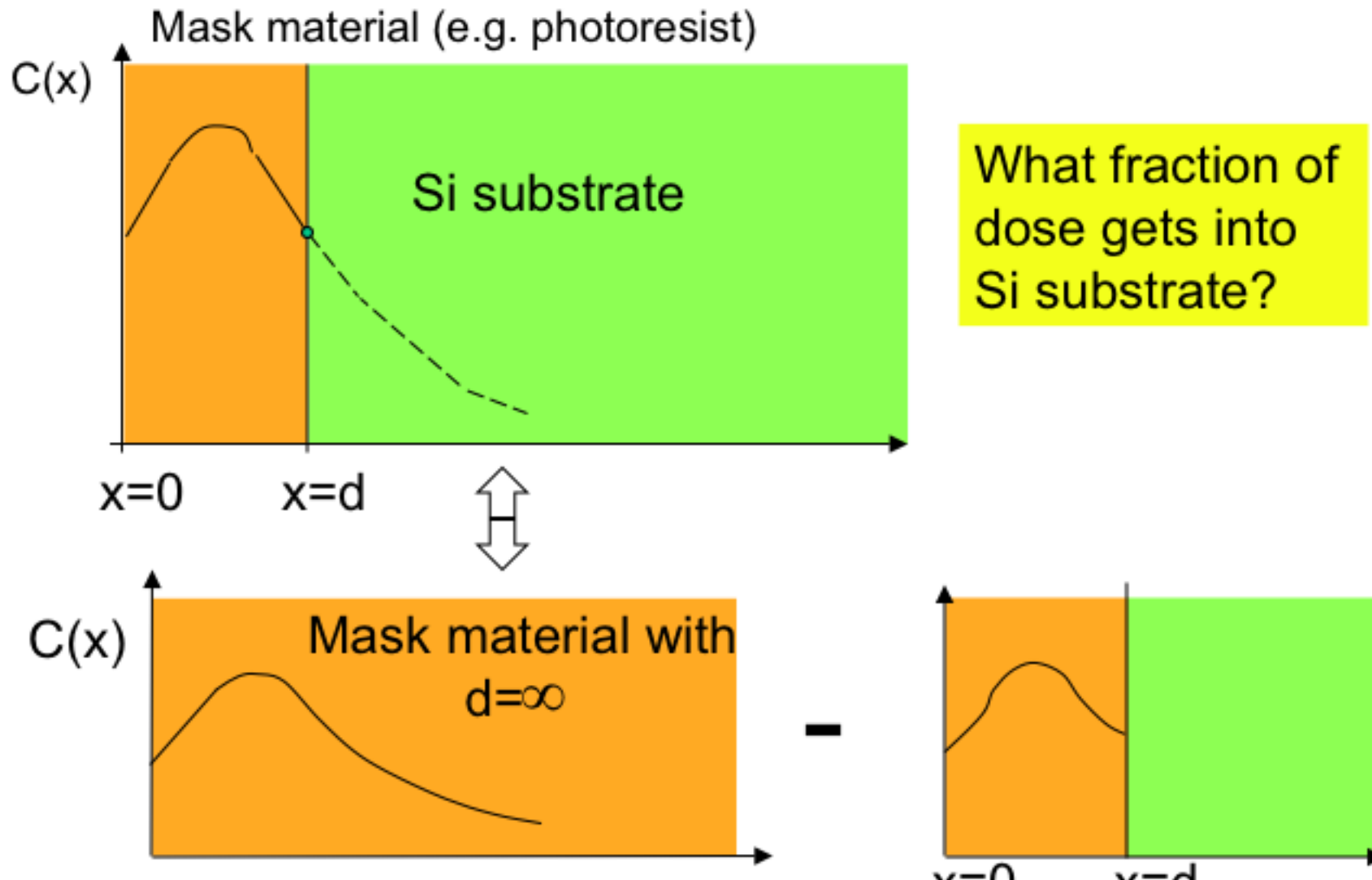
(3) Dual Pearson-IV Distribution



- 9 profile parameters have to be specified:
- $f(x) = f_1(x) + f_2(x)$
- Used to model implant profiles with slight channeling tails

Implant profiles through masks

Transmission Factor of Implantation Mask



Implant profiles through masks

Transmitted Fraction through a mask of thickness d

$$T = \int_0^\infty C(x)dx - \int_0^d C(x)dx$$
$$= \frac{1}{2} erfc \left\{ \frac{d - R_p}{\sqrt{2}\Delta R_p} \right\}$$

$R_p, \Delta R_p$
are values of
for ions into
the **masking material**

$$erfc(x) = 1 - \frac{2}{\sqrt{\pi}} \int_0^x e^{-y^2} dy$$

Rule of thumb: Good masking thickness

$$d = R_p + 4.3\Delta R_p$$

$$\frac{C(x=d)}{C(x=R_p)} \sim 10^{-4}$$

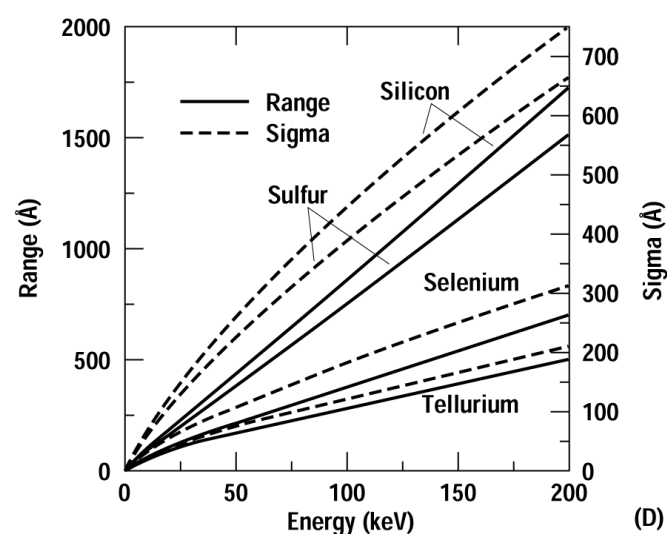
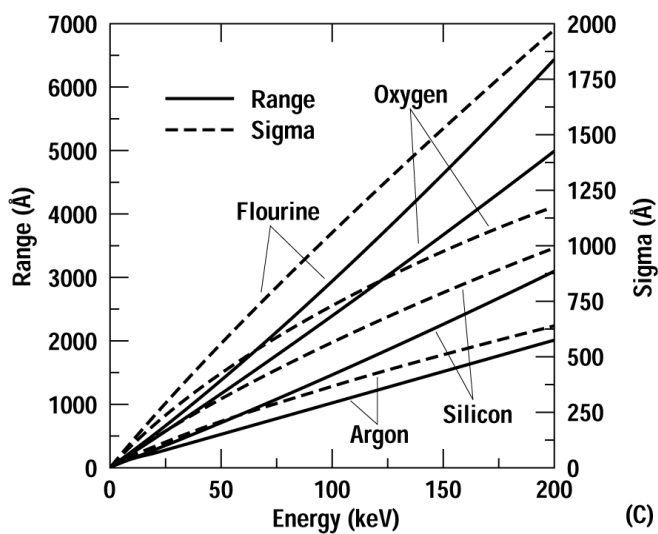
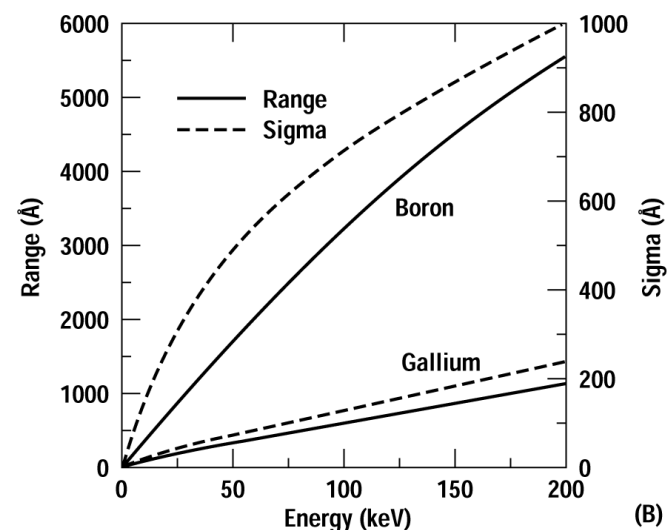
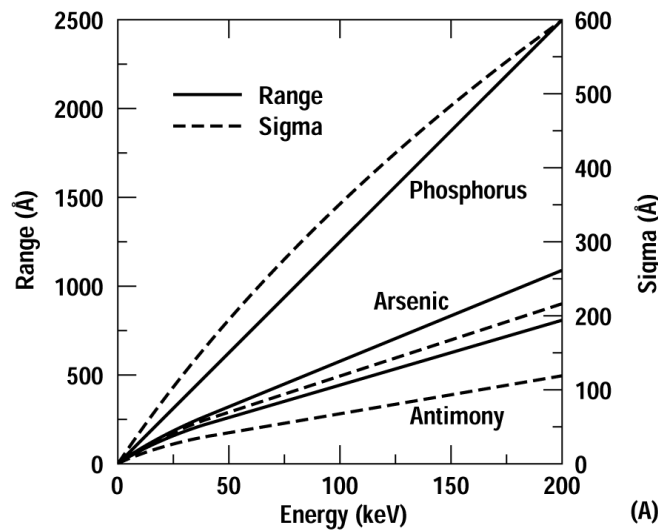


Figure 5.9 Projected range (solid lines and left axis) and standard deviation (dashed lines and right axis) for (A) n-type, (B) p-type, and (C) other species into a silicon substrate, and (D) n-type and (E) p-type dopants into a GaAs substrate, and several implants into (F) SiO_2 and (G) AZ111 photoresist (data from Gibbons *et al.*).

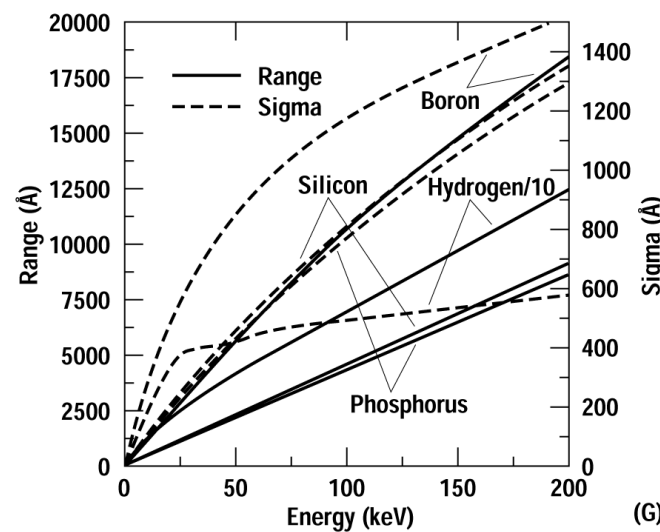
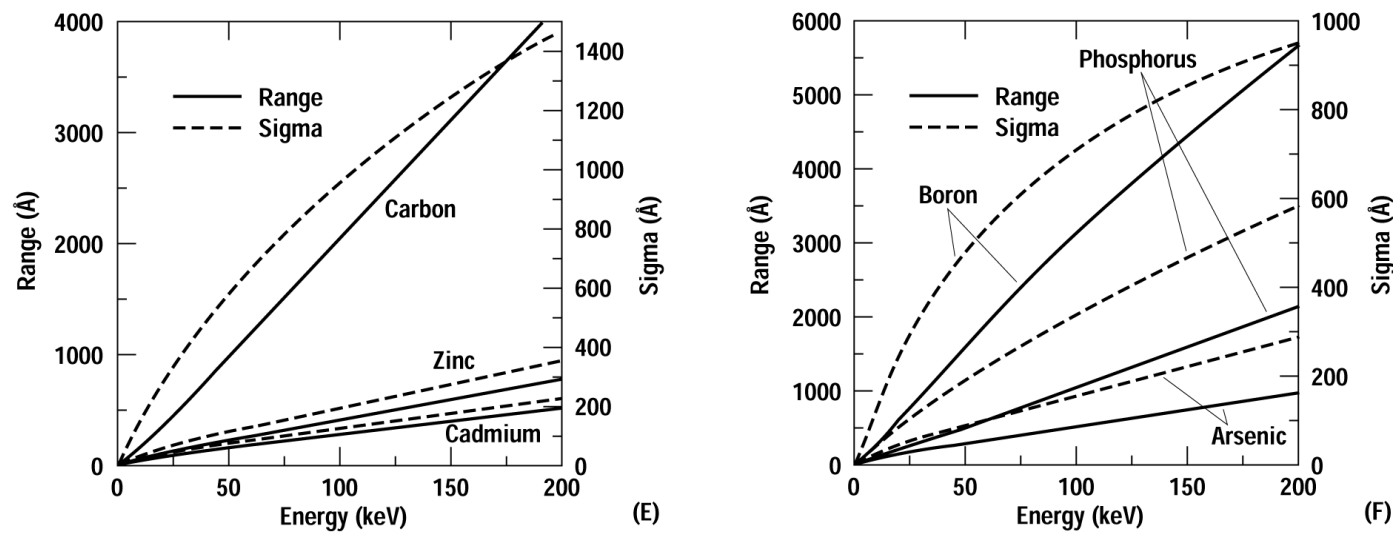
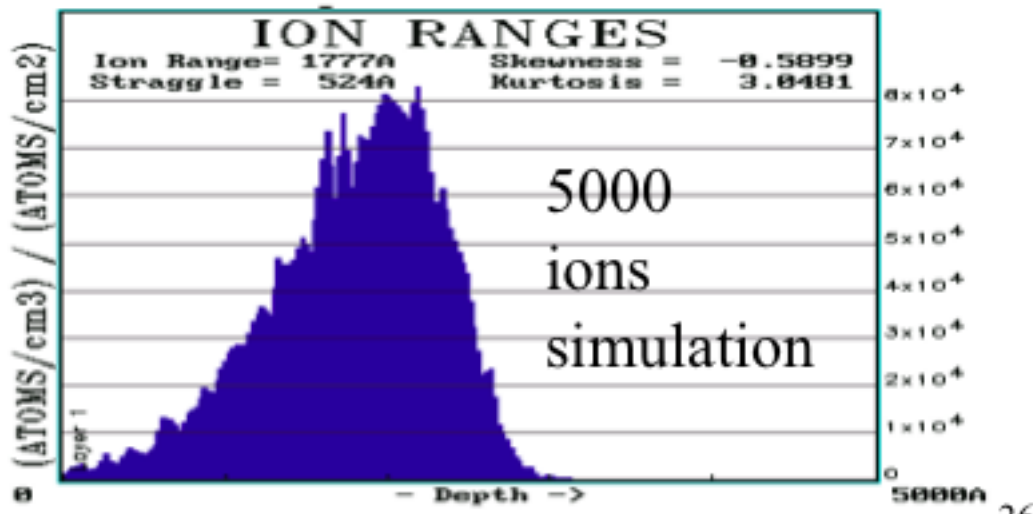
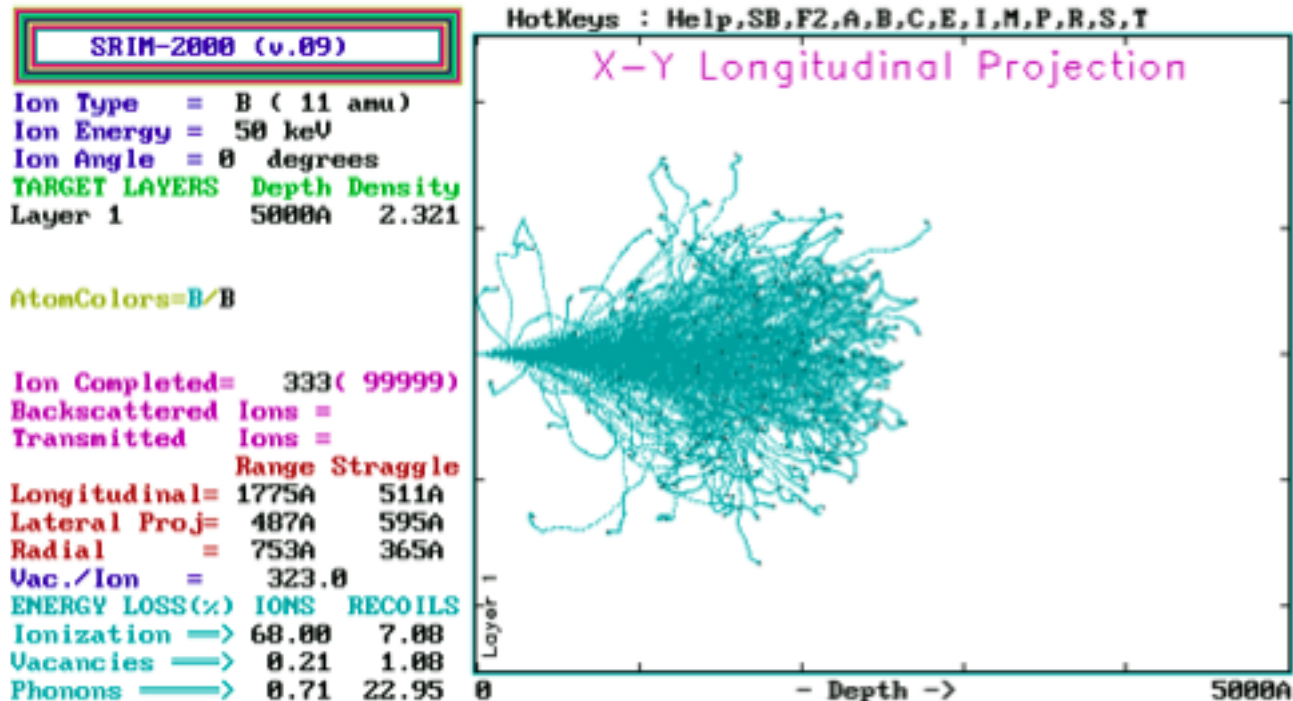


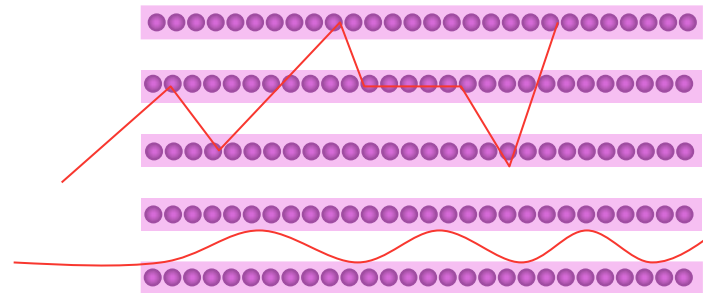
Figure 5.9 cont'd. For legend see previous page.

Monte Carlo Simulation of 50keV Boron implanted into Si



SRIM
Simulator

Channeling



Steering of ion, small angle correlations between collisions

Also 'feed in; is possible

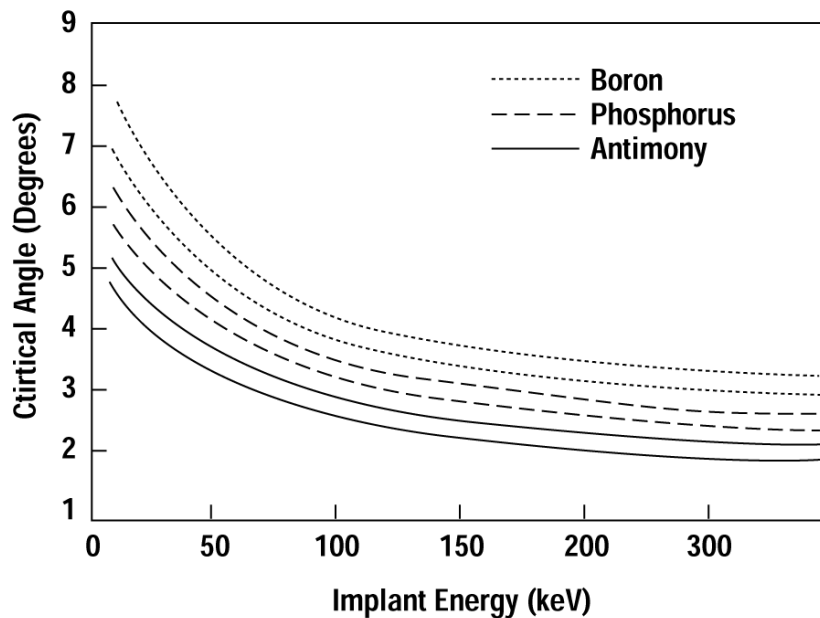
Range becomes larger than in an amorphous material

Critical angle - dependence on E, Z

Low energy largest problem/challenge

Implant in pre-amorphised Si with Si, Si with Ge

channeling



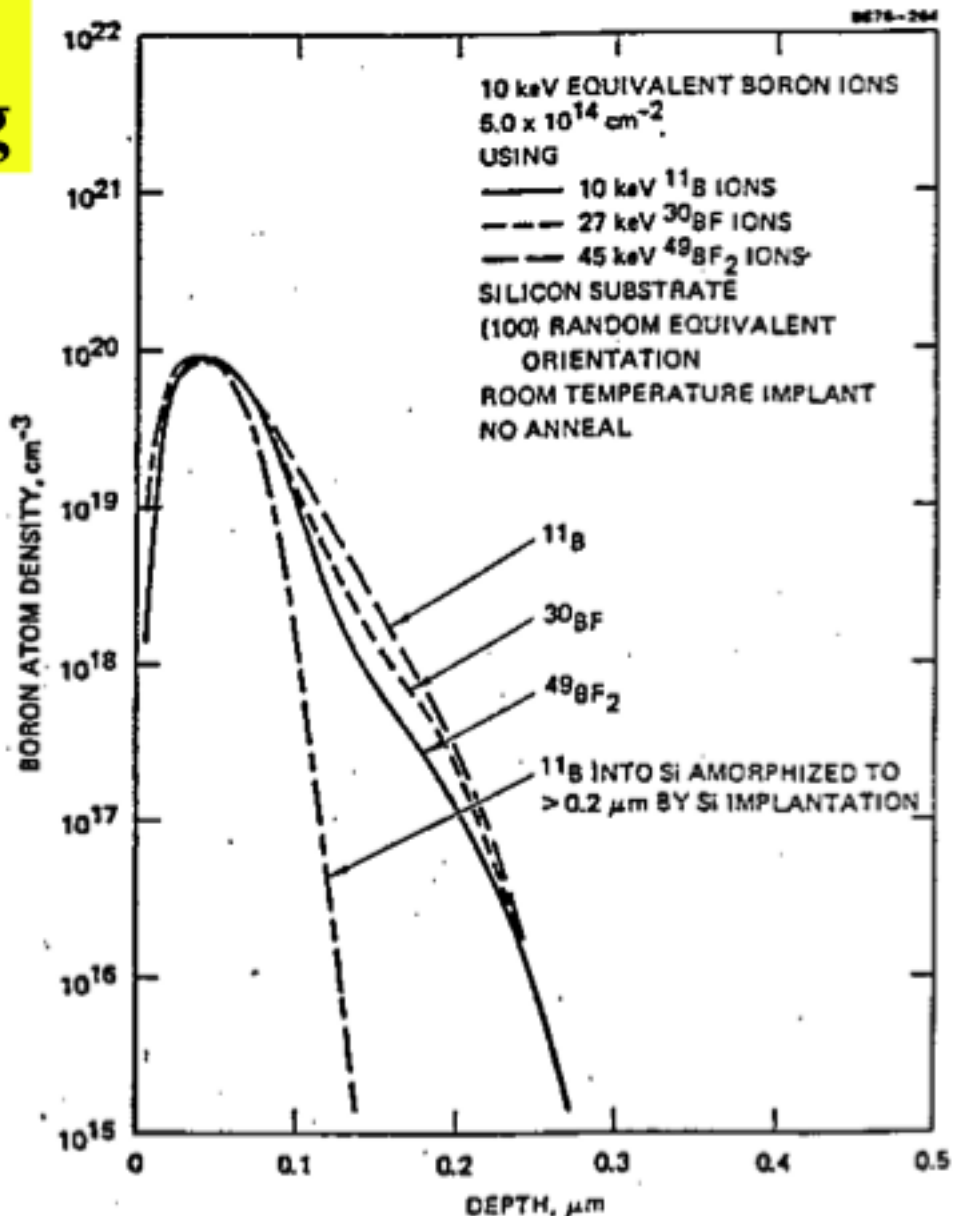
$$E \uparrow \Rightarrow \psi_{crit} \downarrow$$

$$M_1 \uparrow \Rightarrow \psi_{crit} \uparrow$$

Figure 5.12 Critical angle at which channeling begins for common impurities in silicon. For each impurity the upper curve is implanting into $\bar{1}11$ substrates. The lower curves correspond to $\bar{1}00$ substrates.

Pre-amorphization to avoid channeling

- 1) Si substrate preamorphized by Si implantation (dose $\sim 1E15/cm^2$)
- 2) Dopant implantation will experience no channeling



Implantation disorder

Caused by elastic collisions

$\Delta t = 10^{-13}$ sec, 10^{-12} thermal equilibrium, 10^{-9} reordering

Boron loss -mostly inelastic at start of trajectory.

Most displacement close to the end

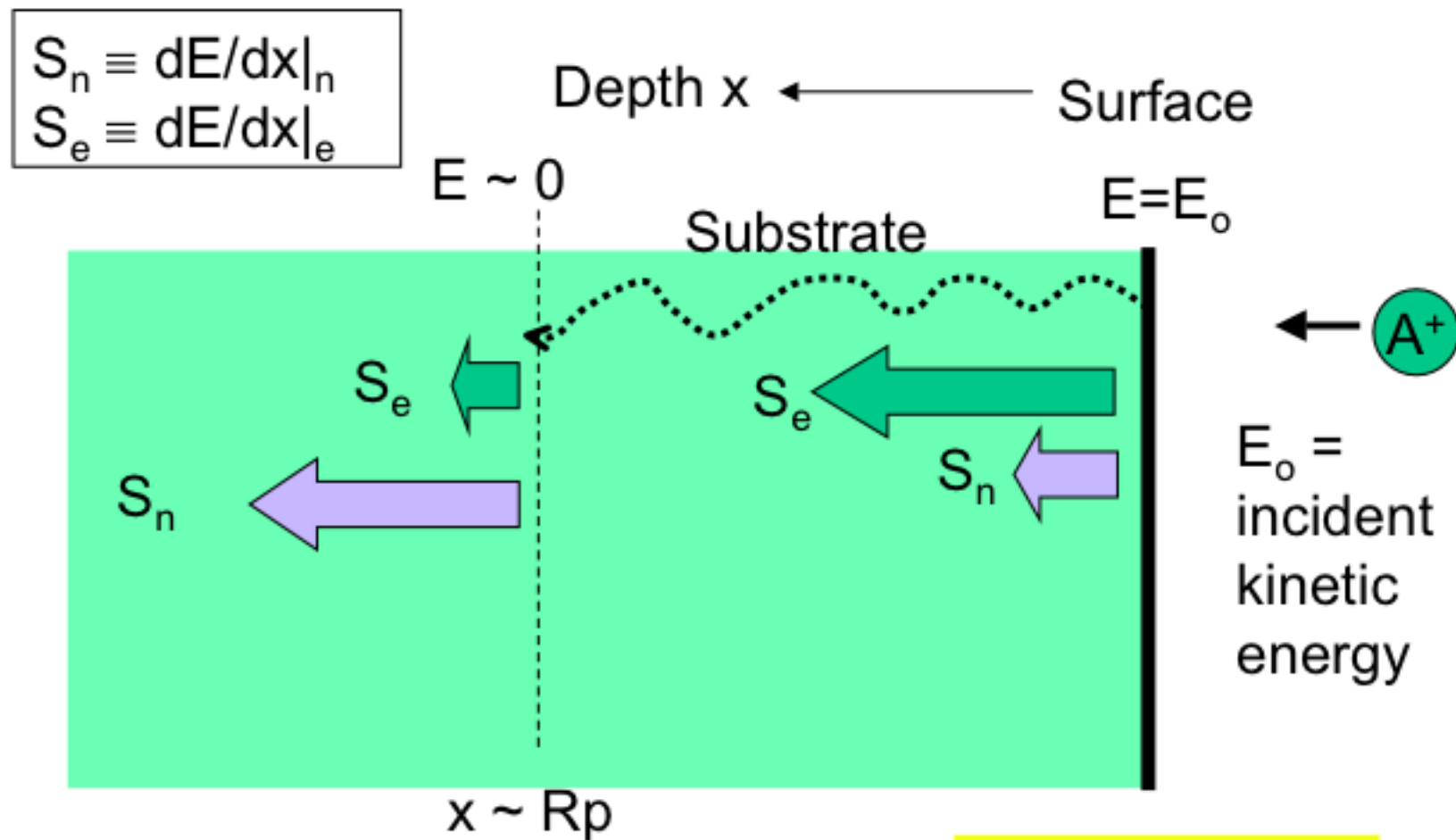
Arsenic starts large elastic loss, disorder similar to As distribution

Density displaced atoms = Dose/Energy * S_n

$F_{\text{disorder}} > F_{\text{amorphous}}$ \rightarrow amorph

Buried amorphous layer

Damage distribution



More crystalline
damage at end of
range $S_n > S_e$

Less crystalline
damage
 $S_e > S_n$

Damage distribution

Energy Loss and Ion Properties

Light ions/at higher energy → more electronic stopping

Heavier ions/at lower energy → more nuclear stopping

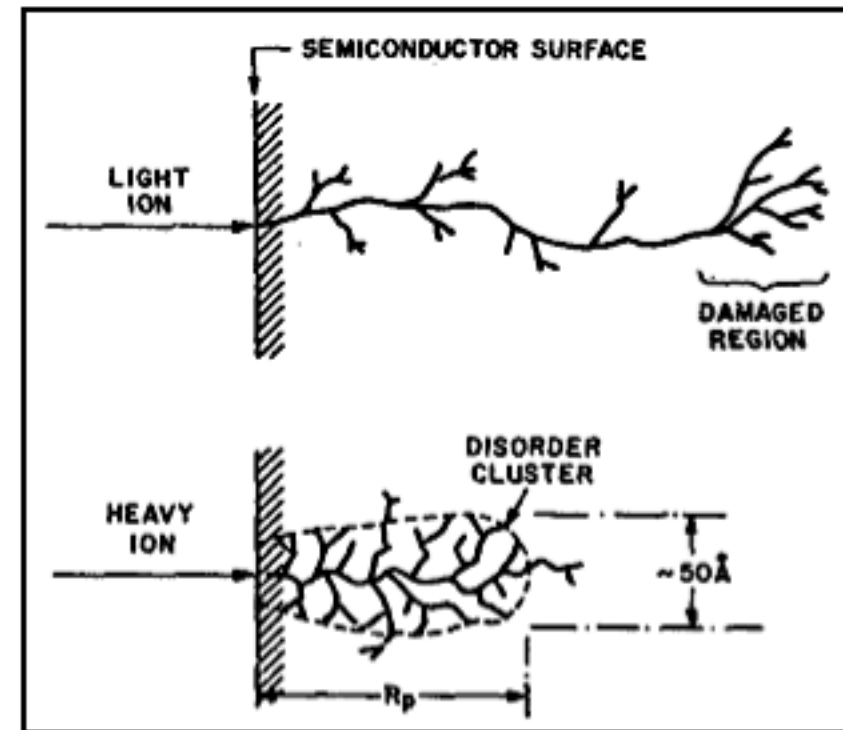
EXAMPLES

Implanting into Si:

H^+ → Electronic stopping dominates

B^+ → Electronic stopping dominates

As^+ → Nuclear stopping dominates



Damage profile

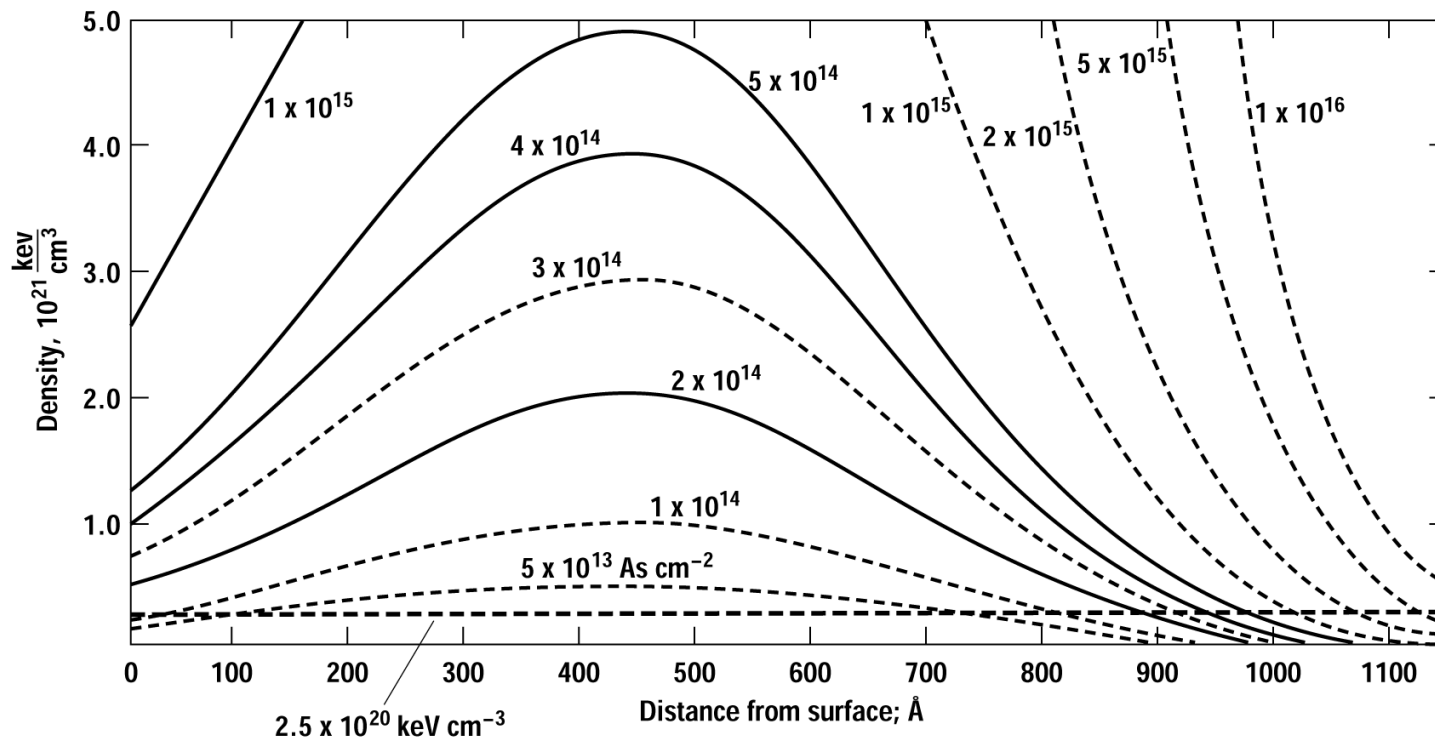


Figure 5.16 Damage density distribution for 100 keV arsenic implanted into silicon with dose as a parameter (reprinted by permission, AIP, after Prussin *et al.* [21]).

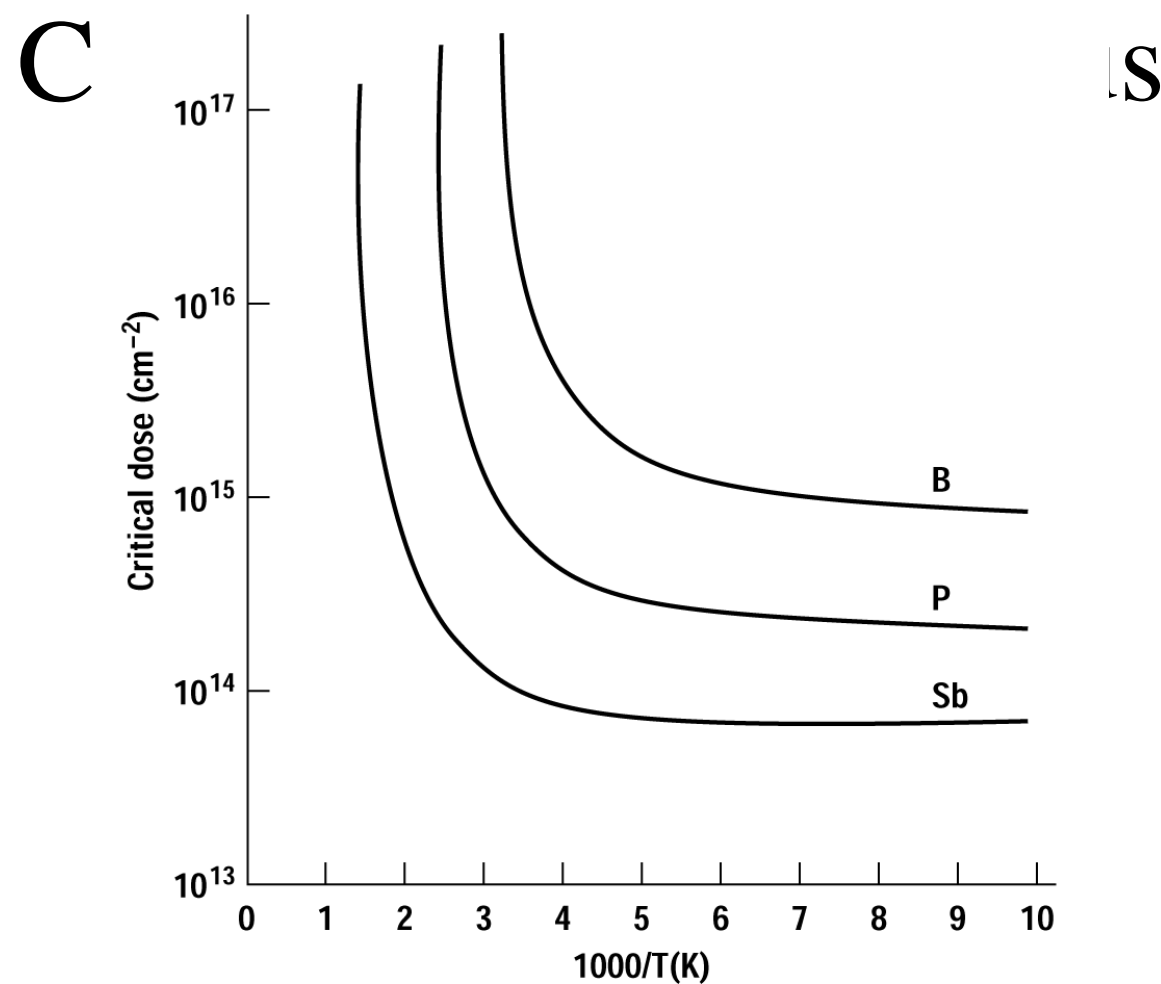


Figure 5.13 Critical implant dose required to amorphize a silicon substrate as a function of substrate temperature for several common silicon dopants (*after Morehead and Crowder*).

Annealing

Amorphous anneals different than
non amorphous

Amorphous -SPEG

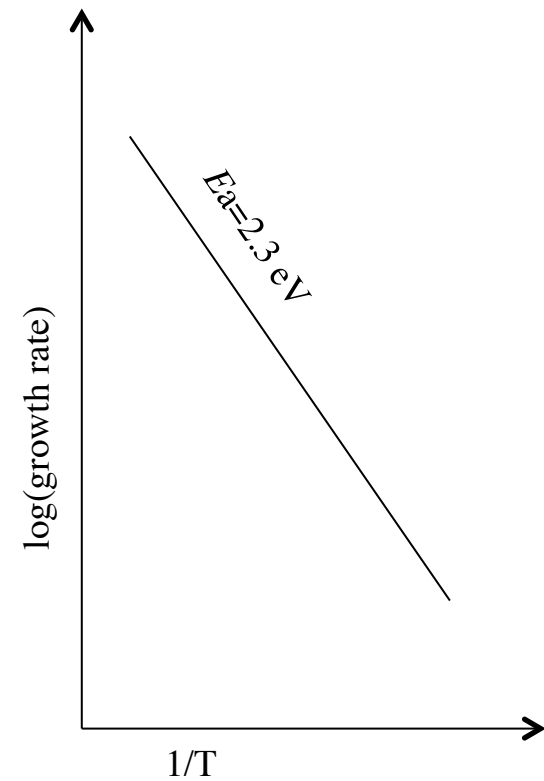
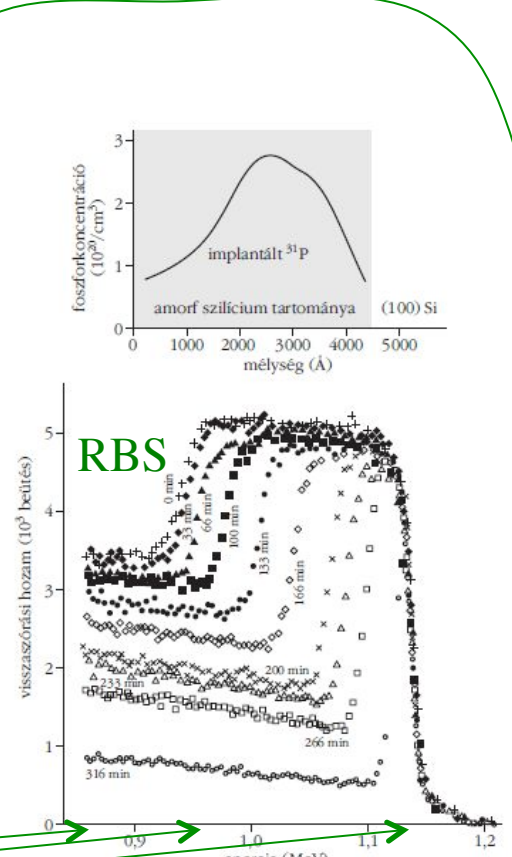
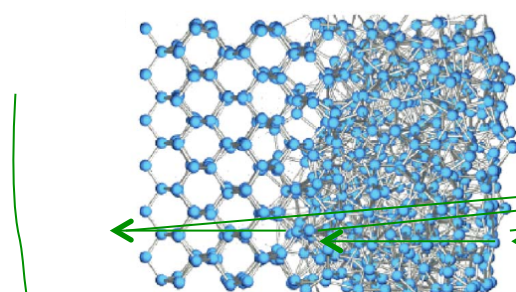
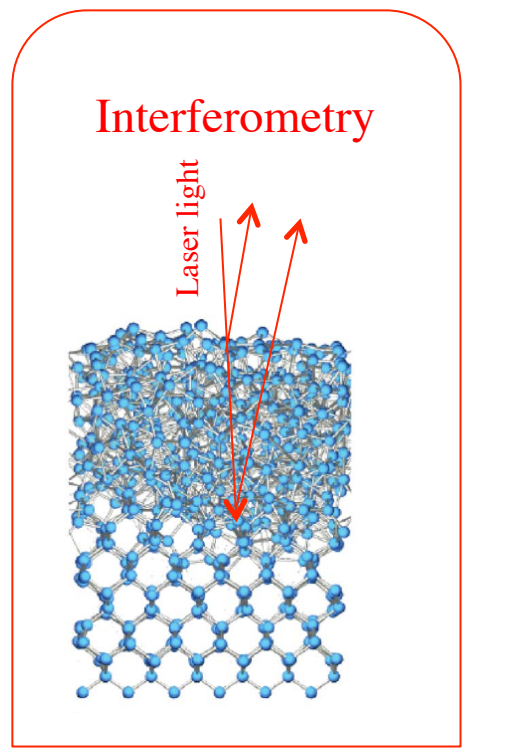
Epi growth , Δx prop t , $\Delta E_a = 2.3$ eV, collective bond flipping

Two-stage annealing

Ion straggling disorder

SPEG solid phase epitaxial growth

Measurement of growth velocity



SPEG

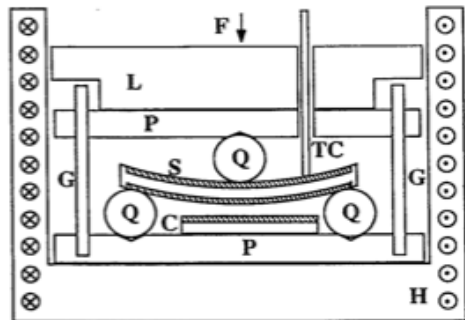


FIG. 1. Schematic cross section of three-point bending apparatus for annealing wafers under nonhydrostatic stress. Sample, cross-hatched areas correspond to amorphous calibration sample; Q: fused quartz support rods; P: brass G: guide posts; TC: thermocouple; H: heating element; W: weights; L: lid.

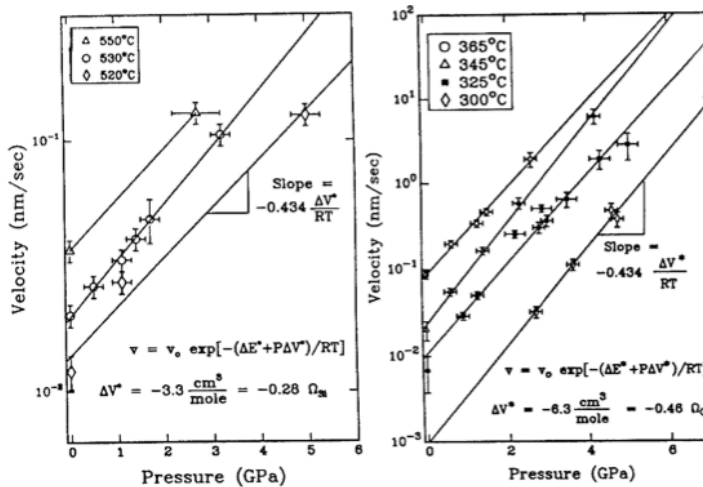


FIG. 1. Hydrostatic pressure enhancement of Solid Phase Epitaxial Growth rate in pure Si (left) and Ge (right).

$$v = v_0 \exp\left(-\frac{\Delta E^*}{kT}\right) \exp\left(-\frac{P\Delta V^*}{kT}\right),$$

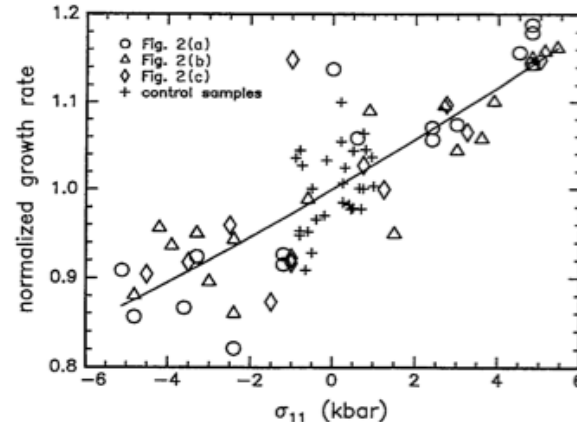
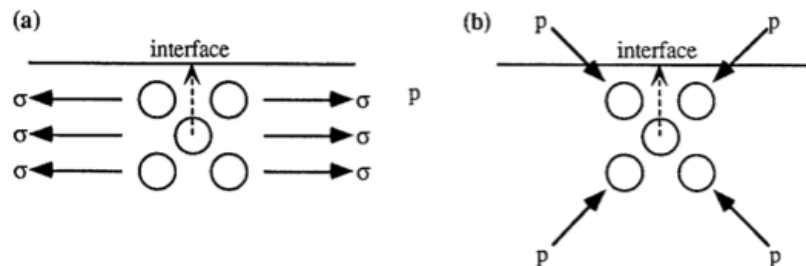


FIG. 3. Variation of growth rate with applied stress for all samples. Open symbols correspond to high-stress samples in Fig. 2. Scatter in data can be reduced by taking into consideration controls and the trends evident from Fig. 2, but such manipulations are not necessary to obtain an approximate magnitude for the stress effect. Curve is fit to Eq. (7) with $\Delta V_{11}^* = 0.15\Omega$.

ic analogue of the activation volume, is developed to characterize such measurements. The measurement permits us to characterize to first order the entire activation strain tensor for solid-phase epitaxy of Si(001): The transition state for this process involves an in-plane expansion and a contraction in the direction normal to the interface. Its symmetry is inconsistent with all proposed bulk point-defect mechanisms.

SPEG

$$v \propto \frac{k_d \cdot k_i}{k_d + k_i},$$



Although the SPEG process occurs by motion of a sharp c/a interface, models conflict on whether the process is controlled by interface reaction kinetics^{12,13} or by bulk diffusion of defects to the interface^{2,6,14-17}. Lu *et al.* addressed both possibilities; their analysis is summarized below.

unlikely alternative is that they have identical activation energies - and volumes). In SPEG of Si, the single activation energy over 10 decades in velocity³ offers strong evidence for a single significantly rate-limiting step. If the limiting step is the interface reaction then it is not really a bulk defect mechanism. In this case, how defects are transported to the interface becomes almost as peripheral a question as how thermal energy is transported to the atoms in the reaction. If,

pressure study of Ge self-diffusion. The clear difference between their result and the negative activation volume obtained by Lu *et al.* in Ge shows that Eq. (3) is violated, hence the defects that limit self-diffusion in the crystal and those limiting the SPEG rate are not the same.

Implications for Vacancies in Si. Despite extensive research on diffusion in Si, whether the diffusion process is mediated by interstitials or vacancies remains open. No definitive measurement exists of the activation volume for self diffusion. A recent total energy calculation by Antonelli and Bernholc²⁶ of pressure effects on Si self-diffusion yielded a vacancy formation volume of

SPEG

TABLE 1. Candidate point defects governing crystal growth and conclusions regarding tenability of mechanisms.

Defect Governing SPEG	Authors	Conclusions
Defects residing at c/a interface		
Dangling bonds	Spaepen and Turnbull ^a	Plausible
Kink sites	Williams and Elliman ^b	special case of dangling bond mechanism
Defects residing in crystal		
Vacancies	Csepregi <i>et al.</i> ^c , Suni <i>et al.</i> ^d	Highly Implausible (Si); Impossible (Ge)
Interstitials		Highly Implausible
Defects residing in amorphous		
Dangling bonds	Mosley <i>et al.</i> ^e	Impossible
Floating bonds	Pantelides ^f	Impossible
any other point defect in amorphous phase	Narayang, Licoppe and Nissim ^{g,h}	Impossible

^aSee ref. 12.

^bSee ref. 13.

^cSee ref. 2.

^dSee ref. 6.

^eSee ref. 15.

^fSee ref. 16.

^gSee ref. 14.

^hSee ref. 17.

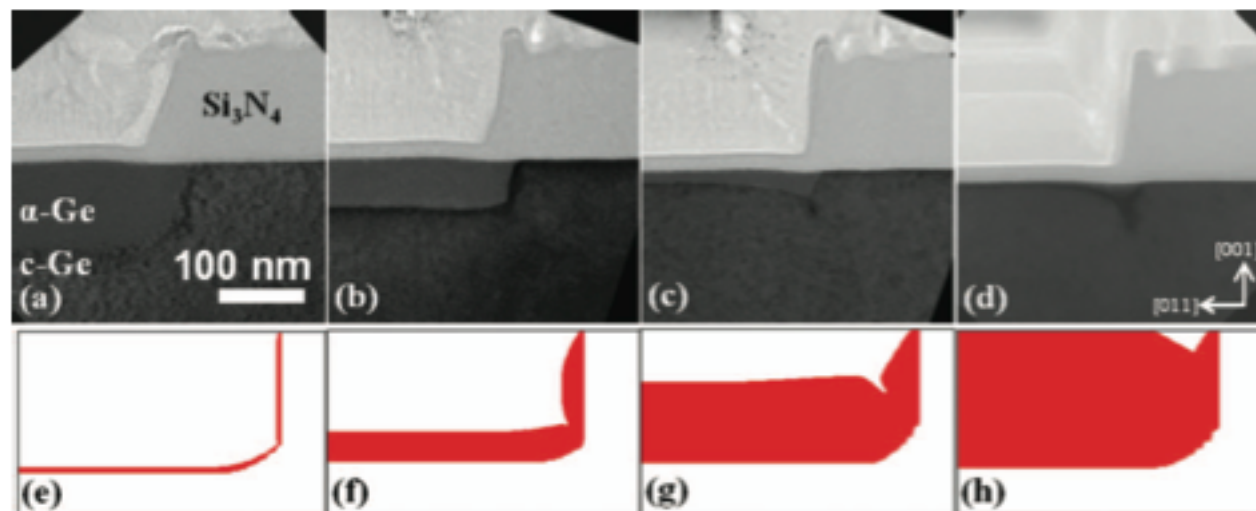


Figure 2. Cross sectional TEM images of nitride stressed patterned Ge implanted with 90 keV 5×10^{14} Ge⁺/cm² and annealed at 330°C for (a) 0, (b) 44, (c) 135, and (d) 235 minutes. The corresponding FLOOPS simulations are shown below in (e) through (h) using a curvature factor of $A = 8 \times 10^{-8}$ cm. A mask edge defect is produced in the stressed case.

SPEG

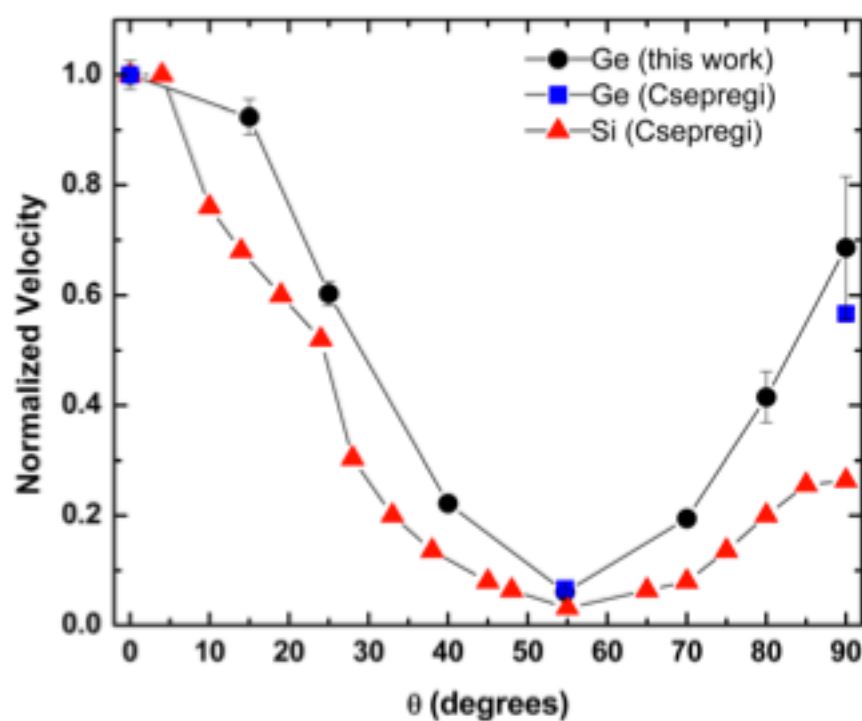


FIG. 7. SPEG velocities normalized to the [001] direction for Ge in this work compared with normalized literature values for Ge and Si. Csepregi used RBS to measure SPEG velocities for Si at 550 °C and Ge at 331.5 °C.^{9,10}

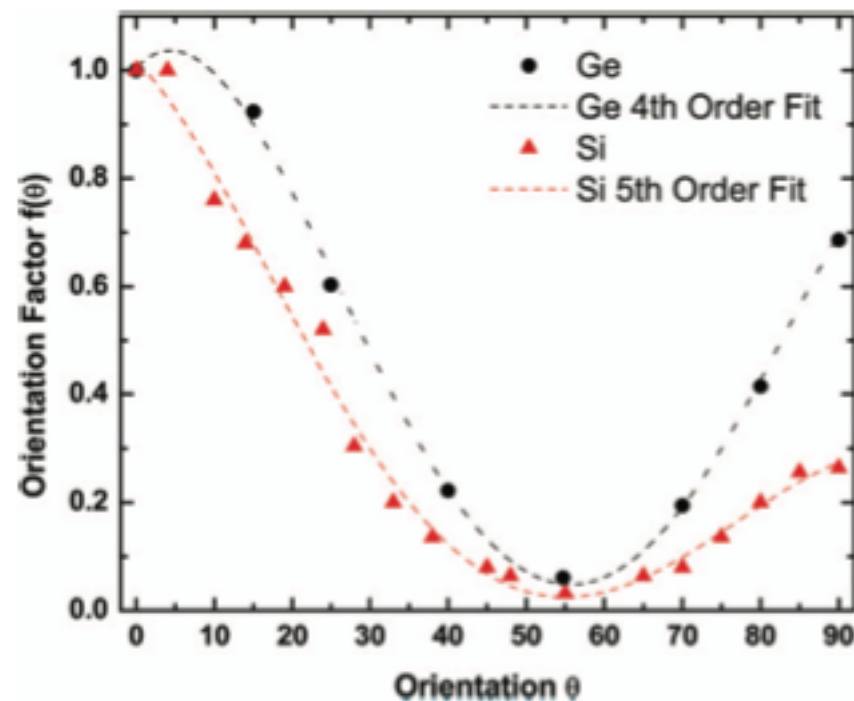


Figure 1. The Ge and Si orientation dependence on SPEG velocities normalized to the [001] direction (0°). A 4th order fit was given to the Ge data,¹⁶ while a 5th order fit was given to the Si data.²³ The [111] and [011] directions exist at 54.7° and 90°, respectively.

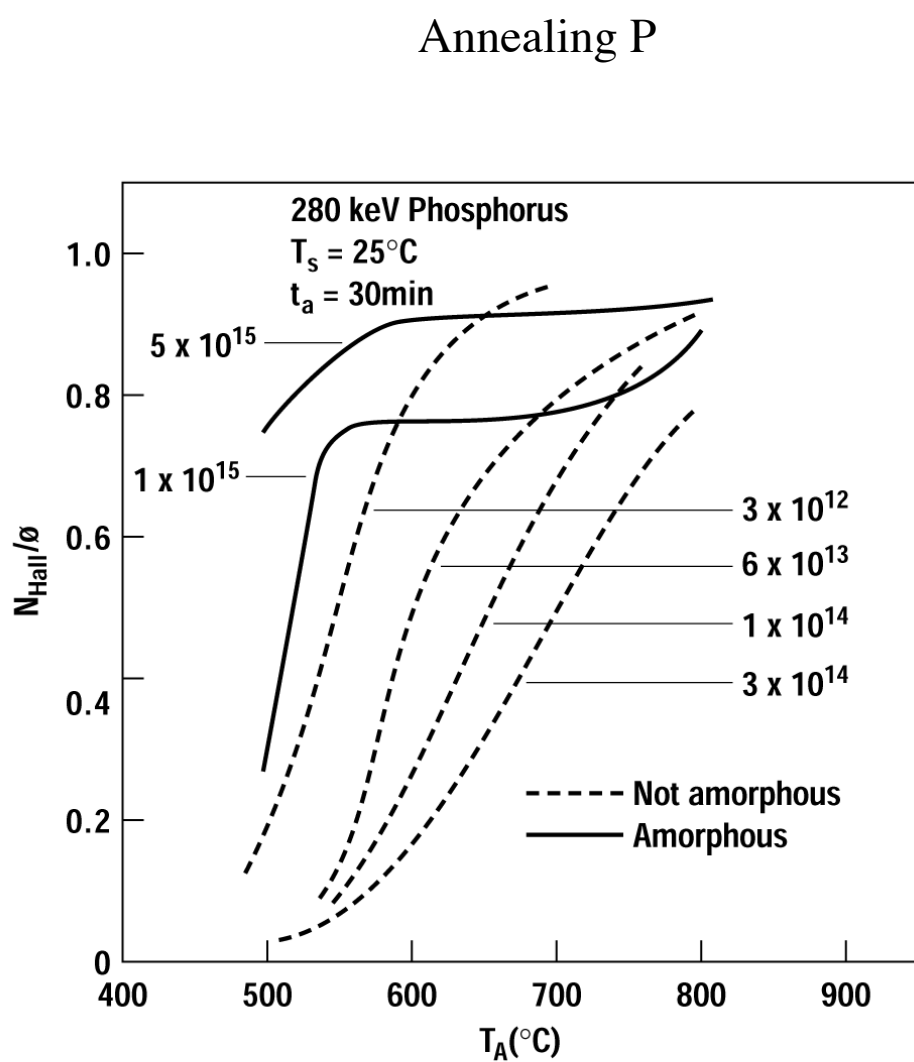


Figure 5.17 Isochronal annealing of phosphorus in silicon, with dose as a parameter. The solid lines correspond to implants that amorphized the substrate (*reprinted by permission, AIP, after Crowder and Morehead*).

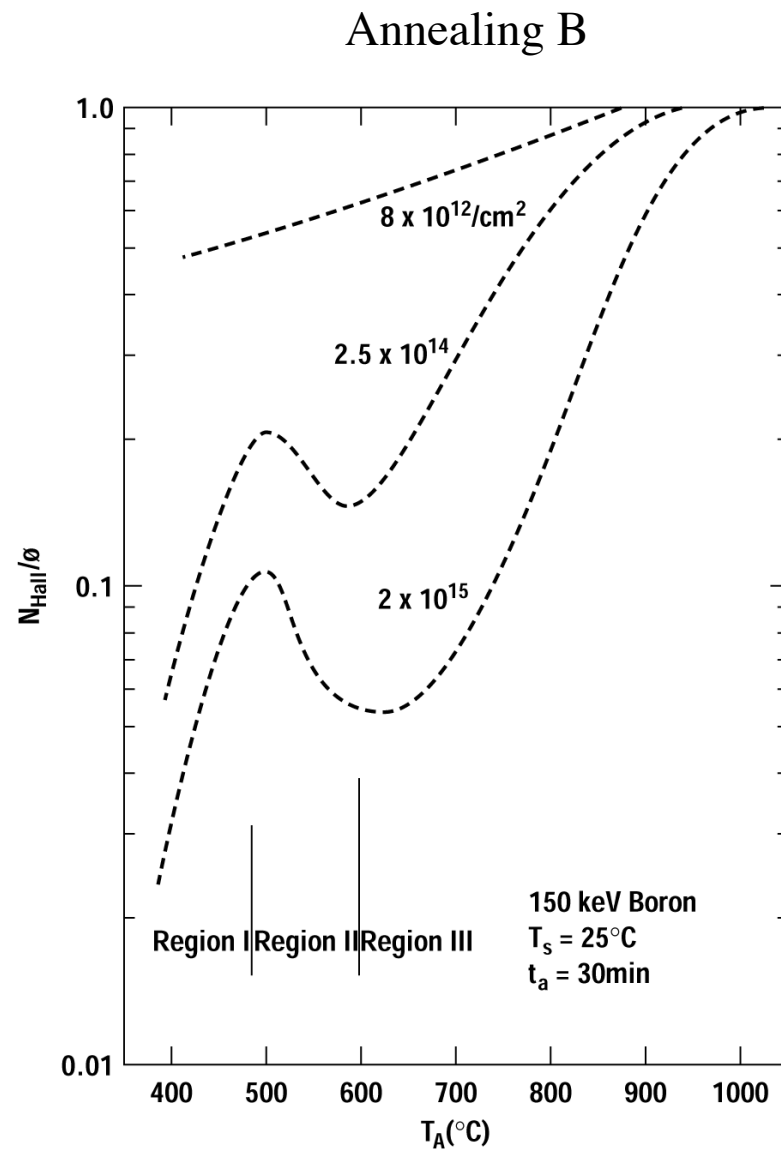
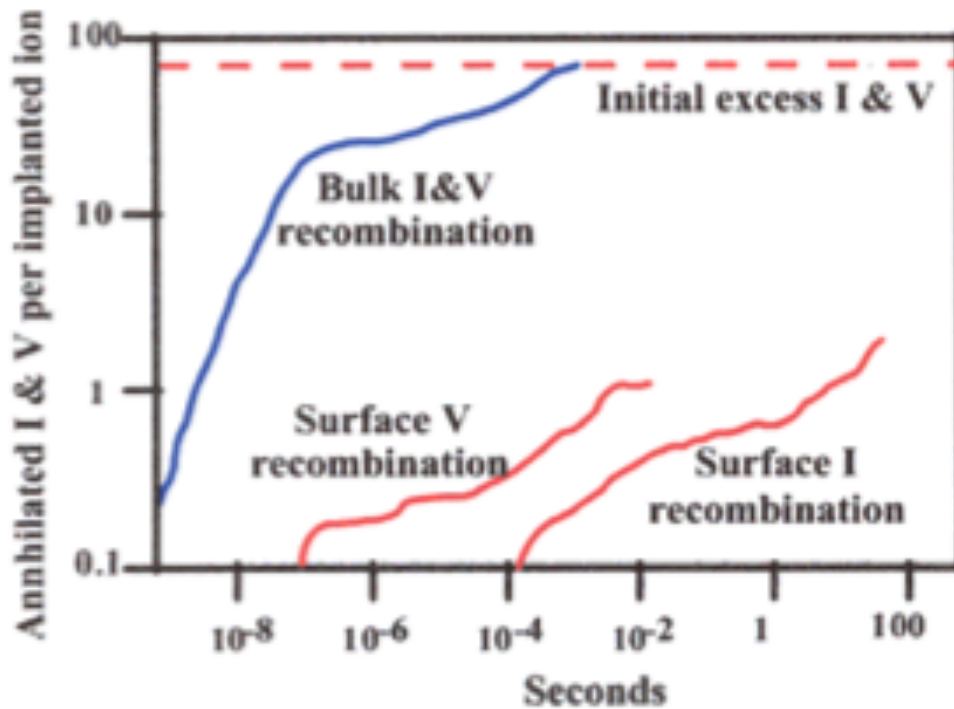


Figure 5.15 Fraction of implanted boron activated in silicon for several isochronal anneals (*after Seidel and MacRae, reprinted by permission, Elsevier Science*).

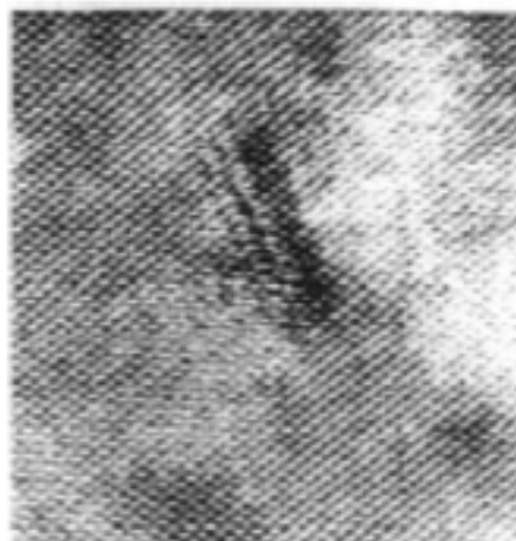
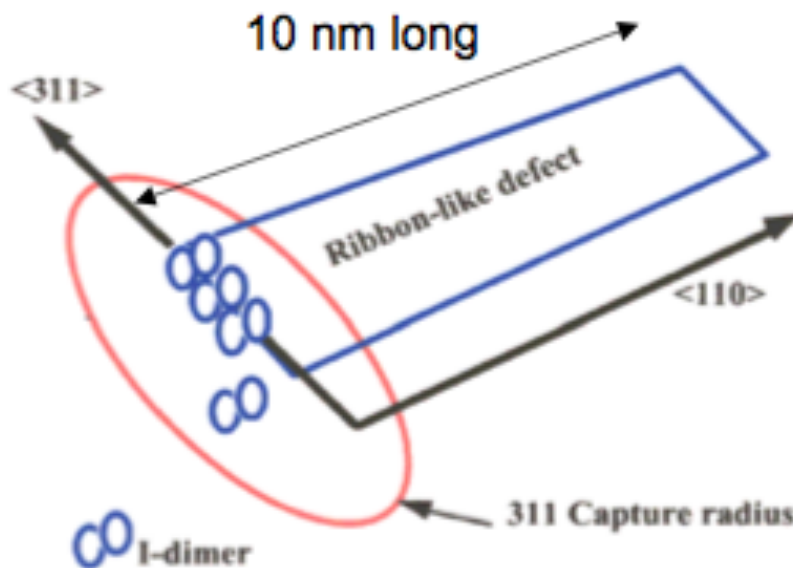
Damage Evolution



Monte Carlo simulation of I & V recombination. After short time, only excess I remain, and these form clusters in a fraction of a second at 800C.

- Bulk and surface recombination take place on a short time scale.
- "+1" I excess remains. These I coalesce into {311} defects which are stable for longer periods.

{311} Defects



{311} defects capture I and form clusters

- {311} defects anneal out in sec - min at moderate temperatures (800 - 1000°C) but eject I \Rightarrow TED.

Below a certain damage value, these {311} defects can dissolve completely.

Above this damage level, can turn into stable dislocation loops which are more difficult to remove.